



HAL
open science

Localized General Vertical Coordinates for Quasi-Eulerian Ocean Models: The Nordic Overflows Test-Case

Diego Bruciaferri, Catherine Guiavarc'H, Helene T Hewitt, James Harle,
Mattia Almansi, Pierre Mathiot, Pedro Colombo

► **To cite this version:**

Diego Bruciaferri, Catherine Guiavarc'H, Helene T Hewitt, James Harle, Mattia Almansi, et al.. Localized General Vertical Coordinates for Quasi-Eulerian Ocean Models: The Nordic Overflows Test-Case. *Journal of Advances in Modeling Earth Systems*, 2024, 16, 10.1029/2023ms003893 . hal-04693964

HAL Id: hal-04693964

<https://hal.science/hal-04693964>

Submitted on 11 Sep 2024

HAL is a multi-disciplinary open access archive for the deposit and dissemination of scientific research documents, whether they are published or not. The documents may come from teaching and research institutions in France or abroad, or from public or private research centers.

L'archive ouverte pluridisciplinaire **HAL**, est destinée au dépôt et à la diffusion de documents scientifiques de niveau recherche, publiés ou non, émanant des établissements d'enseignement et de recherche français ou étrangers, des laboratoires publics ou privés.



Distributed under a Creative Commons Attribution - NonCommercial - NoDerivatives 4.0
International License



RESEARCH ARTICLE

10.1029/2023MS003893

Localized General Vertical Coordinates for Quasi-Eulerian Ocean Models: The Nordic Overflows Test-Case

Key Points:

- A general methodology to embed distinct types of vertical coordinates in local time-invariant targeted areas of quasi-Eulerian ocean models
- Three different hybrid geopotential/terrain-following coordinates are localized in the Nordic overflows region of a z^* -levels global model
- Using local multi-envelope terrain-following levels reduces diapycnal mixing improving the realism of the simulated Nordic overflows

Supporting Information:

Supporting Information may be found in the online version of this article.

Correspondence to:

D. Bruciaferri,
diego.bruciaferri@metoffice.gov.uk

Citation:




Bruciaferri, D., Guiavarc'h, C., Hewitt, H. T., Harle, J., Almansi, M., Mathiot, P., & Colombo, P. (2024). Localized general vertical coordinates for quasi-Eulerian ocean models: The Nordic overflows test-case. *Journal of Advances in Modeling Earth Systems*, 16, e2023MS003893. <https://doi.org/10.1029/2023MS003893>

Received 19 JUN 2023

Accepted 1 FEB 2024

Author Contributions:

Conceptualization: Diego Bruciaferri, Catherine Guiavarc'h, Pierre Mathiot
Formal analysis: Diego Bruciaferri
Funding acquisition: Helene T. Hewitt
Investigation: Diego Bruciaferri, Catherine Guiavarc'h
Methodology: Diego Bruciaferri, James Harle

Diego Bruciaferri¹ , Catherine Guiavarc'h¹, Helene T. Hewitt¹ , James Harle², Mattia Almansi^{2,3} , Pierre Mathiot⁴, and Pedro Colombo^{4,5}

¹Met Office Hadley Center, Exeter, UK, ²National Oceanography Centre, Southampton, UK, ³Now at B-Open Solutions srl, Rome, Italy, ⁴Université Grenoble Alpes, CNRS, IRD, Grenoble INP, Grenoble, France, ⁵Now at University of New South Wales, Sydney, NSW, Australia

Abstract A generalized methodology to deploy different types of vertical coordinate system in arbitrarily defined time-invariant local areas of quasi-Eulerian numerical ocean models is presented. After detailing its characteristics, we show how the general *localization* method can be used to improve the representation of the Nordic Seas overflows in the UK Met Office NEMO-based eddy-permitting global ocean configuration. Three z^* -levels with partial steps configurations localizing different types of hybrid geopotential/terrain-following vertical coordinates in the proximity of the Greenland-Scotland ridge are implemented and compared against a control configuration. Experiments include a series of idealized and realistic numerical simulations where the skill of the models in computing pressure forces, reducing spurious diapycnal mixing and reproducing observed properties of the Nordic Seas overflows are assessed. Numerical results prove that the localization approach proposed here can be successfully used to embed terrain-following levels in a global geopotential levels-based configuration, provided that the localized vertical coordinate chosen is flexible enough to allow a smooth transition between the two. In addition, our experiments show that deploying localized terrain-following levels via the multi-envelope method allows the crucial reduction of spurious cross-isopycnal mixing when modeling bottom intensified buoyancy driven currents, significantly improving the realism of the Nordic Seas overflows simulations in comparison to the other configurations. Important hydrographic biases are found to similarly affect all the realistic experiments and a discussion on how their interaction with the type of localized vertical coordinate affects the realism of the simulated overflows is provided.

Plain Language Summary Numerical ocean models are arguably one of the most advanced tools the scientific community can use to study the dynamics of the world's oceans. However, the ability of an ocean model to realistically simulate ocean currents depends on the numerical techniques it employs, such as the type of vertical coordinate system. Ocean models typically implement a single type of vertical coordinate throughout the entire model domain, which is often unable to accurately represent the vast variety of physical processes driving the oceans. In this study, we propose a new method that allows different types of vertical coordinates in selected regions of the same model domain. Our method targets a particular class of ocean models (known as quasi-Eulerian), improving the way they represent the important influence the sea floor exerts on ocean currents. After introducing our novel approach, we present the results of a series of numerical experiments where we test its skill for improving the representation of the Nordic Seas overflows, an important type of ocean current located at depth in the proximity of the Greenland-Scotland ridge.

1. Introduction

The governing equations of modern numerical ocean models are typically formulated in terms of a generalized vertical coordinate (GVC) $s = s(x, y, z, t)$ (e.g., Adcroft & Campin, 2004; Adcroft et al., 2019; Bleck, 2002; Griffies, 2012; Leclair & Madec, 2011; Petersen et al., 2015; Shchepetkin & McWilliams, 2005), where the only constraint for s is to be a strictly monotone function of the depth z (e.g., Griffies, 2004; Kasahara, 1974). In general, GVCs usually employed in numerical ocean models can be divided in three main groups, depending on the algorithm applied to treat the vertical direction when time-stepping the oceanic equations (e.g., Adcroft & Hallberg, 2006; Griffies et al., 2020; Leclair & Madec, 2011): quasi-Eulerian (QE; e.g., Kasahara, 1974), Lagrangian (LG; e.g., Bleck, 2002) and Arbitrary Lagrangian Eulerian (ALE; e.g., Hirt et al., 1974) coordinates.

Models using QE coordinates diagnose the vertical advective velocities from mass continuity. Because such an approach of treating the vertical direction applies both to classical Eulerian (i.e., time-invariant) z -coordinates as

Project administration: Helene T. Hewitt
Software: Diego Bruciaferri, James Harle, Mattia Almansi
Supervision: Helene T. Hewitt
Validation: Diego Bruciaferri
Visualization: Diego Bruciaferri
Writing – original draft: Diego Bruciaferri
Writing – review & editing: Diego Bruciaferri, Catherine Guiavarc'h, Helene T. Hewitt, James Harle, Mattia Almansi, Pierre Mathiot, Pedro Colombo

well as to those vertical coordinates that can move with the barotropic motion of the ocean, this class of GVCs is defined “*quasi*”-Eulerian. Examples of the latter type of QE coordinates are the rescaled geopotential z^* -coordinate (Adcroft & Campin, 2004; Stacey et al., 1995), the various types of terrain-following coordinates (e.g., Phillips, 1957; Shchepetkin & McWilliams, 2005; Song & Haidvogel, 1994) and subsequent hybridization of these two ($z^* - \sigma$ coordinates; e.g., Bruciaferri et al., 2018; Dukhovskoy et al., 2009; Wise et al., 2021). The second type of GVCs are the LG coordinates; the practical realization of this type of GVC takes advantage of vertical Lagrangian-remap methods to evolve the computational surfaces with the flow whilst retaining a grid able to provide an accurate representation of the ocean state, as in modern isopycnal models (e.g., Adcroft et al., 2019; Bleck, 2002). Lastly, and providing the most general framework, are the ALE coordinates, such as the \tilde{z} -coordinate proposed by Leclair and Madec (2011) and Petersen et al. (2015) or the adaptive terrain-following γ -coordinates of Hofmeister et al. (2010). Models adopting this class of GVCs employs vertical ALE methods to modify the computational grid in time with a motion that typically does not strictly mimic the oceanic flow (i.e., in a Lagrangian sense), but can follow any prescribed algorithm.

In the continuous limit, oceanic equations formulated in different GVCs are of course completely equivalent. However, numerical discretization can introduce errors specific to the type of GVC employed that can seriously undermine the ability of a numerical model to accurately represent some aspects of the oceanic dynamics, especially on climatic scales (e.g., Griffies, Böning, et al., 2000; Haidvogel & Beckmann, 1999). One such example is the inevitable truncation errors that arise from the tracer advection schemes, causing substantial spurious diapycnal mixing in the ocean interior of QE models. This leads to a modification of water masses and potentially significant climatic model drifts (Griffies, Böning, et al., 2000; Griffies, Pacanowski, & Hallberg, 2000). It has been demonstrated that the same type of numerical mixing can be greatly reduced when using LG or ALE vertical coordinates (e.g., Adcroft et al., 2019; Megann et al., 2022).

The choice of GVC also dictates the way an ocean model resolves the bottom topography, hence affecting its ability to simulate the critical interactions between flow and topography. In the case of QE geopotential coordinates, the step-like nature of the sea floor in the ocean model can compromise the accuracy of the simulated large scale ocean dynamics (e.g., Ezer, 2016; Penduff et al., 2007). In addition, with z -like coordinates, gravity currents are represented as a combination of lateral-advection and vertical diffusion processes, introducing significant spurious mixing in the simulated bottom intensified flows (Ezer & Mellor, 1994; Legg et al., 2006, 2009; Winton et al., 1998) and in the interior of the ocean when the grid aspect ratio is not adequate to resolve the topographic slope (Colombo et al., 2020). With an improved representation of the sea floor, as in the case of QE terrain-following coordinates, flow-topography interactions are more naturally simulated and such deficiencies can be substantially reduced (e.g., Ezer, 2005, 2016; Käse, 2003; Schoonover et al., 2016; Willebrand et al., 2001). However, employing QE terrain-following coordinates in regions of steep topography can introduce significant errors in the computation of horizontal pressure forces, making their use in global configurations challenging (e.g., Lemarié et al., 2012). The use of isopycnal coordinates has been proven to be effective in reducing spurious mixing in idealized (Legg et al., 2006) and realistic simulations of the Nordic Seas overflows (Guo et al., 2016; Megann et al., 2010; H. Wang et al., 2015). However, such models suffer from the outcropping of coordinate interfaces in weakly stratified regions, detrainment from a mixed layer into the ocean interior and difficulties in representing a non-linear equation of state and parameterizing diapycnal mixing (e.g., Griffies, Böning, et al., 2000; Megann et al., 2022).

Ocean models typically implement one single type of vertical coordinate throughout the model domain. However, it is evident that a perfect vertical coordinate suitable for *any* oceanic regime does not exist and a hybrid approach, combining the best features of each vertical coordinate system within a single framework, is currently an active area of research. In one such example, Bleck (2002) and subsequently Adcroft et al. (2019) tried to alleviate some of the drawbacks of isopycnal models using a LG hybrid isopycnal- z^* vertical coordinate. Adcroft et al. (2019) reports that issues still remain with the dense high latitude overflows and concludes that more research is needed to determine a robust vertical grid algorithm suitable for the World Ocean. On paper, generalized ALE coordinates appear to be the most attractive framework for evolving in time the vertical grid according to a *dynamical* algorithm that seeks the optimal coordinate configuration for the various oceanic regimes of the model domain. However, the practical realization of such an *optimal* ALE is non-trivial, and active research is currently on-going (e.g., Gibson, 2019; Hofmeister et al., 2010).

To better represent some features of the ocean dynamics such as flow-topography interactions, an algorithm that defines time-invariant target areas of the model domain where the vertical grid smoothly transitions into another more appropriate GVC may be sufficient. This was the concept behind the hybrid vertical coordinate of Timmermann et al. (2012) and Q. Wang et al. (2014): to improve the representation of shelf-deep ocean exchanges and sub-ice-shelf cavities in the Antarctic marginal seas, their global model used terrain-following σ -layers only along the Antarctic shelf and continental slope while z -levels were used in the rest of the domain. Later, Colombo (2018) extended this idea proposing a local-sigma vertical coordinate to improve the representation of the Nordic Seas overflows in a global model. Their methodology allowed the embedding of vanishing quasi-sigma terrain-following levels (Dukhovskoy et al., 2009) in the Greenland-Scotland ridge region of a z^* -coordinates based model. Their study definitely showed the potential of the concept. However, it also pointed out that the development of such a mesh is non-trivial, especially when defining the transition zone between the two vertical coordinates, highlighting some limitations in their method that might preclude its applicability in a more general sense.

Building on the study of Colombo (2018), the aim of this paper is to (a) introduce a general methodology that enables QE numerical ocean models to localize (i.e., embed) various GVCs configurations within a model domain and (b) assess the ability of the new method to improve the representation of the Nordic Seas overflows in eddy-permitting global ocean simulations. Two different types of numerical experiments are conducted in this study. At first, a series of idealized numerical experiments is carried out to test the accuracy of localized GVCs in computing horizontal pressure forces and reproducing gravity currents. After, realistic global simulations are run to test the skill of the localized vertical coordinates in reproducing observed properties of the Nordic Seas overflows when compared with the traditional approach of employing z^* -coordinates with partial steps.

The manuscript is organized as follows. The next Section 1.1 introduces the Nordic Seas overflows and their main oceanographic properties. Section 2, with the help of Appendix A, describes the details of the localization method proposed in this study. Section 3 presents the Nordic overflows test-case, describing the global ocean model used in our integrations and the three localized QE vertical coordinates developed and tested in our experiments (see also Appendix B for more details on the vertical coordinates, Appendix C for a description of the algorithm applied in this study to increase the accuracy of the implemented localized QE grids and Appendix D for some details on the iso-neutral mixing operator). Sections 4 and 5 describe and discuss the set-up and the results of the idealized and realistic numerical experiments conducted in this work, respectively. Finally, Section 6 summarizes our conclusion and discuss future perspectives. For the reader convenience, a list of the acronyms used in this paper is given in Appendix E.

1.1. The Nordic Seas Overflows

The Nordic Seas overflows consist of dense cold waters formed in the Nordic Seas and the Arctic Ocean and flowing south via the Greenland-Scotland ridge in the form of strong gravity currents that form the lower limb of the Atlantic Meridional Overturning Circulation (AMOC; e.g. Dickson & Brown, 1994; Johnson et al., 2019; Østerhus et al., 2019). Two water masses originate from these overflows, namely the Denmark Strait Overflow Water (DSOW) and the Iceland-Scotland Overflow Water (ISOW).

The DSOW flows south via the Denmark Strait (see Figure 1), cascading along the continental slope of the western Irminger Sea (Dickson & Brown, 1994). While descending, the DSOW entrains and mixes with the ambient water encountered along its path, resulting in an approximately doubled transport within a few hundred kilometers downstream of the Denmark Strait sill (Dickson et al., 2008). In the proximity of Cape Farewell, the DSOW turns westward and enters the Labrador Sea as the densest part of the Deep Western Boundary Current (DWBC) (e.g., Hopkins et al., 2019).

The path of the ISOW is more complex (see also Figure 1 for the locations). It crosses the Greenland-Scotland ridge primarily via the Faroe-Shetland channel and the Faroe-Bank channel, although secondary contributions via the Wyville Thomson ridge and the Iceland-Faroe ridge are also important (Østerhus et al., 2019). Once the main branch has passed the Faroe-Bank channel, the ISOW descends along the Iceland-Faroe slope, mixing with waters spilling from the Iceland-Faroe ridge. After, the ISOW proceeds south-westward into the Icelandic basin, flowing along the eastern flank of the Reykjanes ridge and mixing with the surrounding ambient fluid. While early observational studies indicated a reduced importance of mixing and dilution in comparison to the DSOW (Saunders, 1996), recent estimates appear to suggest that entrainment contributes in doubling the ISOW transport

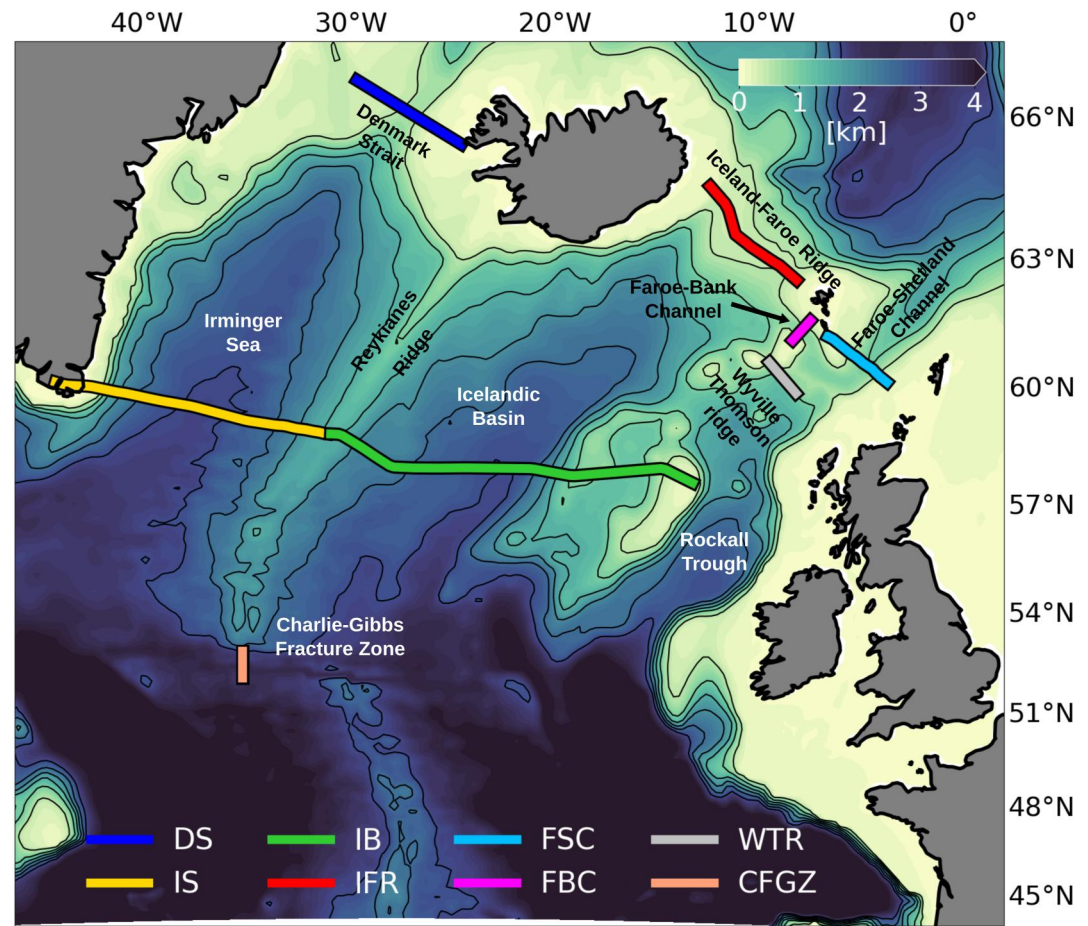


Figure 1. Bathymetry of the Nordic overflows region at $1/4^\circ$ of resolution showing the location of the main geographical features of the area and the position of the observational cross-sections analyzed in the realistic experiments—see Section 5 and Table 1 for the details. The thin black lines are selected isobaths ranging from 500 to 3,000 m with a discretization step of 500 m.

(Johns et al., 2021). The modified ISOW leaves the Icelandic basin through multiple pathways (e.g., Hopkins et al., 2019; S. M. Lozier et al., 2022): on the one side, the dense water descending the Icelandic basin directly flows into the Irminger Sea via various gaps in the Reykjanes ridge; on the other side, after flowing through the Charlie-Gibbs Fracture Zone, the modified ISOW either continues westward spreading toward the Labrador Sea or enters the Irminger sea as a deep boundary current that flows cyclonically around the continental slope of the Irminger basin and rides above the DSO to form the lightest part of the DWBC.

2. Localized Quasi-Eulerian Vertical Coordinates

The intent of developing localized GVCs is to provide ocean models with the capability of arbitrarily varying the vertical coordinate system in targeted areas of the model domain. Although the broad idea of changing/adapting the vertical grid within an ocean model is not new (e.g., Adcroft et al., 2019; Bleck, 2002; Colombo, 2018), the approach proposed here combines three specific attractive features:

- (1) It uses a generalized algorithm to combine any type of QE coordinates in time-invariant limited areas of the model domain;
- (2) It allows for minimal modifications to the original code of an oceanic model;
- (3) It adds small extra computational cost to the simulation (mainly linked to the number of active “wet” cells in the localized area and the scheme chosen for computing horizontal pressure forces) and it does not require any regridding procedure to avoid drifting of the vertical grid as in modern LG models (e.g., Adcroft et al., 2019) or some type of ALE coordinates (e.g., Gibson, 2019; Megann et al., 2022);

Some of these properties follow from the fact that the method introduced here targets QE GVCs, exploiting some key features of this specific class of vertical coordinates. In the next two sections, first the QE approach is summarized (Section 2.1) and after the details of the localization algorithm are described (Section 2.2).

2.1. The Quasi-Eulerian Approach to Vertical Coordinates

The QE approach applies to any GVCs where the vertical coordinate transformation can be expressed as a direct function of the ocean free-surface $\eta(x, y, t)$. The evolution in time of QE coordinate interfaces is importantly controlled by the prognostic thickness equation. In the case of an incompressible Boussinesq ocean, the continuous thickness equation can be written in terms of a GVC $s = s(x, y, z, t)$ and in conservation form as (e.g., Bleck, 1978; Burchard et al., 1997; Griffies et al., 2020)

$$\frac{\partial z_s}{\partial t} + \nabla_s \cdot (z_s \mathbf{u}) + \frac{\partial w}{\partial s} = 0, \quad (1)$$

where $z_s = \partial_s z$ is the Jacobian of the coordinate transformation, $\nabla_s = (\partial_x^s, \partial_y^s, 0)$ is the lateral gradient operator acting along surfaces of constant s , $\mathbf{u}(x, y, s, t)$ is the horizontal flow vector and $w(x, y, s, t) = z_s D_t s$ is the dia-surface velocity (with D_t the material time derivative operator; see Griffies (2004) for the details).

When moving to a discrete level, the transformed vertical domain can be divided into N layers $k = 1, \dots, N$, so that the k th generic model layer is bounded by generalized coordinate interfaces $s_{k+\frac{1}{2}}$ at the top and $s_{k-\frac{1}{2}}$ at the bottom, respectively. In such a framework, the thickness $h_k(x, y, t)$ of the discrete layer k is given by

$$h_k = \int_{s_{k-\frac{1}{2}}}^{s_{k+\frac{1}{2}}} z_s(x, y, s, t) ds = z_{k+\frac{1}{2}} - z_{k-\frac{1}{2}}, \quad (2)$$

where $z_{k\pm\frac{1}{2}}(x, y, t) = z(x, y, s_{k\pm\frac{1}{2}}, t)$ and $z_{k+\frac{1}{2}} > z_{k-\frac{1}{2}}$. This definition ensures that $\int_{s(z=-H)}^{s(z=\eta)} z_s ds = \sum_{k=1}^N h_k = H + \eta$, with $H(x, y)$ the ocean bottom topography and $z_{\frac{1}{2}} = -H(x, y)$ at the bottom boundary and $z_{N+\frac{1}{2}} = \eta(x, y)$ at the free surface. Consequently, the layer integrated thickness equation reads

$$\frac{\partial h_k}{\partial t} + \nabla_s \cdot (h_k \mathbf{u}_k) + w_{k+\frac{1}{2}} - w_{k-\frac{1}{2}} = 0, \quad (3)$$

where $\mathbf{u}_k(x, y, t) = h_k^{-1} \int_{s_{k-\frac{1}{2}}}^{s_{k+\frac{1}{2}}} z_s \mathbf{u} ds$ is the layer averaged horizontal flow vector and $w_{k\pm\frac{1}{2}}(x, y, t) = w(x, y, s_{k\pm\frac{1}{2}}, t)$.

The QE algorithm includes two steps to integrate Equation 3. At first, the thickness tendency is deduced from a prescribed functional relationship of the type $\partial_t h_k \propto \partial_t \eta$, sometimes referred to as the *coordinate equation* (e.g., Leclair & Madec, 2011) since it completely depends on the analytical formulation of the coordinate transformation. Subsequently, once $\partial_t h_k$ is known, the thickness Equation 3 is used to diagnose the dia-surface velocity w .

Introducing a time-invariant model layer thickness $h_k^0(x, y)$ defined for an unperturbed ocean at rest (i.e., when $\eta = 0$) allows one to express the layer thickness as

$$h_k = h_k^0 + \alpha_k \eta, \quad (4)$$

where $0 \leq \alpha_k \leq 1$ represents the ratio of the rate of change of each $h_k(x, y, t)$ to the change rate of $\eta(x, y, t)$. In general this parameter depends on the type of QE vertical coordinate employed. For example, with traditional z -coordinates $\alpha_k = 0$, in early models combining z -levels and a free-surface $\alpha_1 = 1$ (e.g., Dukowicz & Smith, 1994), with the z^* -coordinate of Stacey et al. (1995) and Adcroft and Campin (2004) $\alpha_k = h_k^0 H^{-1}$ while for the s -coordinate of Song and Haidvogel (1994) $\alpha_k = N^{-1}$, with N the number of discrete model levels employed. A useful and attractive approach is to develop a numerical ocean model code that implements vertical coordinate transformations sharing the same formulation for α_k . In such a way, the ocean model can be equipped with a general and relatively simple dynamical core that can be used consistently with different types of QE GVCs. This latter

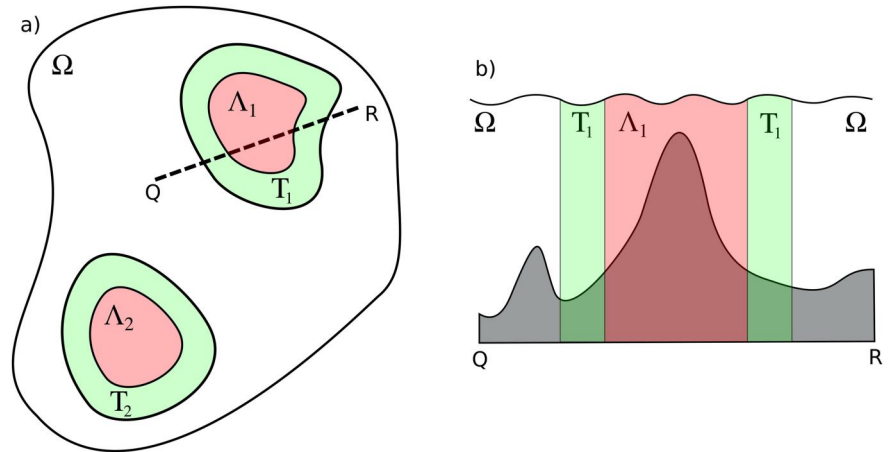


Figure 2. Explanatory sketch of the QE localization method for the case of two localization areas—(a) is a planar view while (b) is a vertical cross-section through line QR. In the white area Ω the model employs the *global* Ω^V QE GVC, while in the two red regions Λ_1 and Λ_2 the *localized* Λ_1^V and Λ_2^V QE coordinates are used. In the green *transition zones* T_1 and T_2 the vertical coordinates T_1^V and T_2^V are computed via Equation 7.

property is particularly useful for the localization method proposed in this paper, as will be explained in the next section.

Modern QE ocean models typically implement vertical coordinates using $\alpha_k = h_k^0 H^{-1}$ (e.g., Adcroft & Campin, 2004; Madec & NEMO-team, 2019; Shchepetkin & McWilliams, 2005), resulting in a QE coordinate equation written as

$$\frac{\partial h_k}{\partial t} = \frac{h_k^0}{H} \frac{\partial \eta}{\partial t} = -\frac{h_k^0}{H} \nabla_s \cdot \int_{s(z=-H)}^{s(z=\eta)} z_s \mathbf{u} ds = -\frac{h_k^0}{H} \nabla_s \cdot \sum_{m=1}^N h_m \mathbf{u}_m, \quad (5)$$

where the free-surface equation (neglecting fresh water sources for simplicity) is used to obtain the second equation.

2.2. The Localization Algorithm

The localization method proposed in this paper permits one to embed distinct *local* QE vertical coordinates in different targeted areas of the same model domain Ω , which otherwise employs the *global* Ω^V QE coordinate system. Figure 2 presents an explanatory sketch for the case of two local areas, although there are no restrictions on the total number P of local areas that can be implemented. Here, the red regions Λ_1 and Λ_2 are two *localization* areas where the model uses Λ_1^V and Λ_2^V QE coordinates, respectively. In addition, the green areas T_1 and T_2 represent *transition zones* where T_1^V and T_2^V vertical coordinates result from a smooth relaxation of the local Λ_1^V and Λ_2^V toward the global Ω^V .

While it is desirable to have complete freedom in choosing the localization areas, it is preferable to apply an algorithm to define the transition regions, since their function is to guarantee the stability of the model solution providing a smooth connection between the two grids. The procedure used for defining the transition areas can be any algorithm able to identify areas of the model domain surrounding the localization regions. For this work we propose a simple method as described in Appendix A.

Once the transition regions have been identified, the following function is used in this study to compute the relaxation weights W_p in the generic transition area T_p (where $1 \leq p \leq P$):

$$W_p = \frac{1}{2} + \tanh\left(\mu_p \frac{D_p - d_p}{D_p + d_p}\right) [2 \tanh(\mu_p)]^{-1}. \quad (6)$$

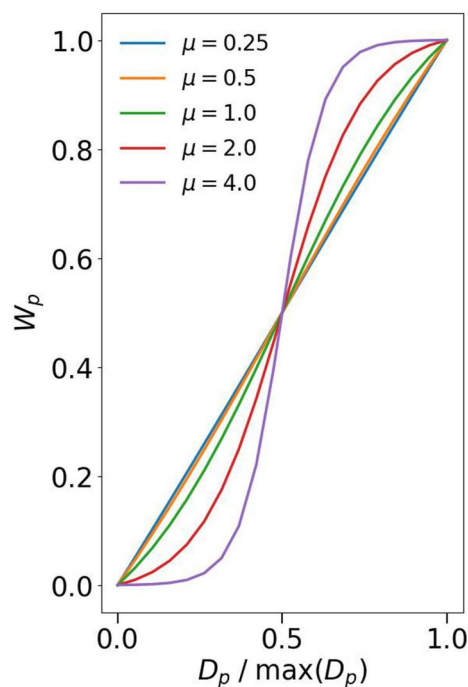


Figure 3. Sensitivity of the W_p distribution (as a function of the normalized distance from the outer boundary D_p) to the μ_p tunable coefficient.

Here, D_p and d_p are the minimum Euclidean distances of a particular point of the transition zone T_p from its outer and inner boundaries, respectively, while $\mu_p = 1.7$ is a tunable coefficient that controls the distribution of W_p as shown in Figure 3.

The global Ω^V as well as the localized Λ_p^V QE coordinate systems are discretized using the same number of vertical levels. Therefore, the thickness h_{k,T_p} of a particular model grid cell included in the area T_p can be computed as

$$h_{k,T_p} = W_p h_{k,\Omega} + (1 - W_p) h_{k,\Lambda_p}, \quad (7)$$

where $h_{k,\Omega}$ and h_{k,Λ_p} are the model grid thicknesses of those cells belonging to either the Ω or the Λ_p zone, respectively, and located right on the boundary with the transition zone.

Equation 4 allows QE ocean models to compute h_k in terms of h_k^0 , α_k and η . Typically, the calculation of h_k^0 is conducted at the very beginning of a model simulation, either as an “off-line” pre-processing step or as a single call in the model code just before the beginning of the time-marching stage. Therefore, if Ω^V and Λ_p^V GVCs use a consistent definition for α_k , the QE localization algorithm can be introduced with minimal changes to the h_k^0 calculation step and no further modifications to the hydrodynamical core of a QE ocean model. In particular, this means that Equation 7 can be used only at the beginning of the simulation to compute h_{k,T_p}^0 . This is particularly convenient since it permits one to detect any vertical grid set-up issue at a very early stage, saving time in the development and implementation process.

The main advantage of the localization method proposed here is that it is fully general and can be applied to blend any type of QE coordinates. Differently, other proposed approaches such as the one of Colombo (2018) can be used to embed only GVCs defined with respect to a single envelope bathymetry and using a single stretching function—for example, classical s - or vanishing quasi-sigma coordinates (vqs, see Section 3.2)—within a z^* -based grid.

Finally, we note that our localization method could be applied also to some type of ALE coordinates, for example, the \tilde{z} -coordinate of Leclair and Madec (2011) and Petersen et al. (2015), where model levels follow the free surface and some type of high-frequency motion (e.g., internal waves). On the other hand, since the simplicity of the method proposed here relies on Equation 4, using the same approach with GVCs where model levels are allowed to vanish (e.g., LG coordinates) seems to be more arduous.

3. The Nordic Overflows Test-Case

In this section, the details of the QE global ocean model used in our numerical experiments (Section 3.1) and the three QE GVCs localized in the proximity of the Greenland-Scotland ridge area (Section 3.2) are given.

3.1. The Eddy-Permitting Global Ocean Model

The numerical integrations described in this manuscript are carried out using a development branch of the GOSI global ocean configuration at $1/4^\circ$ of horizontal resolution (GOSI-025) developed and used by the UK Met Office Hadley Centre and the National Oceanography Centre under the Joint Marine Modeling Program. The GOSI-025 development branch used in this study is an eddy-permitting forced ocean configuration that shares the same physics and parametrizations of the one described in Megann et al. (2022) with few exceptions:

- It is based on version 4.0.4 of the Nucleus for European Modeling of the Ocean (NEMO) numerical ocean model code (Madec & NEMO-team, 2019) instead of version 4.0.1;

- It is forced with the 1958–2020 JRA-55 atmospheric reanalysis (Harada et al., 2016; Kobayashi et al., 2015) instead of the 1948–2006 CORE atmospheric forcing (Large & Yeager, 2009), to cover the observational period (see Section 5);
- It uses the fourth-order FCT scheme for the tracer advection instead of the second order;
- It adopts a formulation for the bottom drag coefficient C_D that is consistent with the “law of the wall” (bottom roughness $z_0 = 3 \times 10^{-3}$ m) for a better representation of the bottom boundary layer dynamics;
- It employs the Griffies et al. (1998) triad formulation for the iso-neutral diffusion since it is the only available option for using iso-neutral mixing with GVCs in the current release of NEMO (see Appendix D for a comparison between this formulation and the one used in the standard GOSI-025);
- It uses the standard NEMO pressure Jacobian scheme (Madec & NEMO-team, 2019) for a more accurate calculation of the horizontal pressure gradient force when using GVCs.

In the vertical direction, GOSI-025 employs the QE z^* -coordinate of Stacey et al. (1995) and Adcroft and Campin (2004) (see Appendix B for the details) discretized using 75 levels and Madec et al. (1996) stretching function. In addition, in order to mitigate inaccuracies affecting the step-like representation of the bottom topography typical of geopotential-based models, the GOSI-025 configuration also employs the Pacanowski et al. (1998) partial step parameterization (see Figure 4b). Hereafter, the control GOSI-025-based configuration employing standard z^* levels with partial steps (z^* ps) everywhere in the domain is referred to as GOSI- z^* ps model.

We note that with the NEMO “log-layer” formulation the bottom drag coefficient C_D is computed as a function of the bottom layer thickness only if \geq of a user defined threshold C_D^{\min} , while is kept constant and equal to C_D^{\min} otherwise (see Madec and NEMO-team (2019) for the details). This latter scenario applies when the bottom vertical resolution is too coarse to resolve the logarithmic layer, condition that typically occurs at depth in geopotential global configurations as GOSI- z^* ps. As a consequence, GOSI- z^* ps uses a bottom friction formulation consistent with the standard GOSI-025 (Storkey et al., 2018).

3.2. Localized General Vertical Coordinates

Vertical coordinates smoothly following the seabed topography are able to offer a more realistic representation of gravity currents than models using geopotential coordinates, both in idealized (e.g., Bruciaferri et al., 2018; Ezer, 2005; Ezer & Mellor, 2004; Ilıcak et al., 2012; Laanaia et al., 2010) and more realistic scenarios (e.g., Colombo, 2018; Ezer, 2006; Käse, 2003; Riemenschneider & Legg, 2007; Seim et al., 2010). Therefore, in this study three different types of QE hybrid geopotential/terrain-following vertical coordinates are localized and tested in the Nordic overflows region.

The localization area developed for this work includes the Greenland-Scotland ridge region and targets (where possible) the 2,800 m isobath (see Figure 4a), the depth at which ∇H decreases (see contour lines shown in Figure 1). In this work, the transition area is defined using the algorithm described in Appendix A. The following are the QE GVCs localized and tested in the Nordic overflows region in this paper:

- *Vanishing quasi-sigma (vqs)*: the vqs method defines vertical coordinates following a smooth envelope topography surface H_e rather than the actual bathymetry H (with $H_e \geq H$), allowing one to reduce the steepness of computational levels with respect to classical terrain-following models (Dukhovskoy et al., 2009). This approach is particularly effective in reducing errors in the computation of horizontal pressure gradients (e.g., Dukhovskoy et al., 2009; O’Dea et al., 2012). However, it can cause “in cropping” of the computational surfaces into the model topography as in z -coordinates, reducing the resolution near the sea bottom and introducing spurious “saw-tooth” patterns in the model bathymetry whenever $H_e - H$ is large, potentially affecting the accuracy of the simulated bottom dynamics. In this study, we implement local vqs vertical coordinates with a similar setting to Colombo (2018) (see Figure 4c, Appendix B, and Figure B1b for the details).
- *Hybrid sz -transitioning (szt)*: the *szt* scheme described in Wise et al. (2021) defines QE levels that follow a smooth envelope bathymetry H_e above a user-defined depth while smoothly transition into z^* -interfaces with partial steps at greater depths, effectively allowing one to combine vqs and z^* QE coordinates. In this study, we configure the local *szt* vertical discretization scheme to use terrain-following levels up to $\approx 1,200$ m (see Figure 4d, Appendix B, and Figure B1c for the details on the configuration).

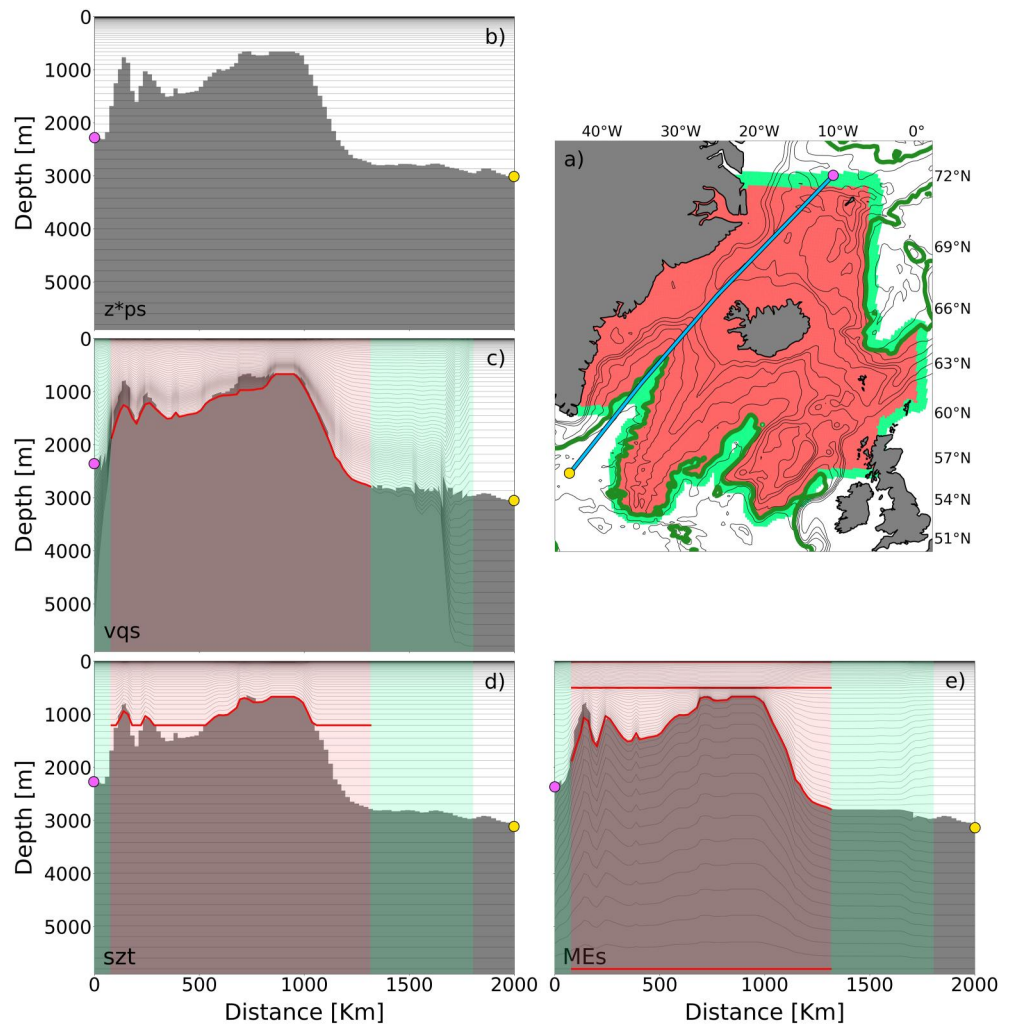


Figure 4. In panel (a) the red and green regions represent the Nordic overflows localization and transition areas used in this study, respectively, while the cyan line shows the location of the model bathymetry cross-sections presented in the other panels and the green line marks the 2,800 m isobath. Panel (b) shows the model bathymetry cross-section extracted from the GOSI- z^*ps configuration, panel (c) from the GOSI- vqs configuration while panel (d) and (e) from the GOSI- szt and GOSI-MEs configurations, respectively. In panels (b–e) the red lines shows the location of the envelopes used to configure the localized GVCs while the magenta and yellow points show the beginning and the end of the cross-sections to indicate the direction of increasing distance in panel (a).

- *Multi-Envelope s-coordinates (MEs)*: the ME method defines QE coordinate interfaces that are curved and adjusted to multiple arbitrarily defined surfaces (aka envelopes) rather than following geopotentials, the actual bottom topography or a single-envelope bathymetry as in the case of vqs or szt GVCs. In such a way, computational levels can be optimized to best represent different physical processes in different sub-domains of the model while minimizing horizontal pressure gradient (HPG) errors (Bruciaferri et al., 2018, 2020, 2022; Wise et al., 2021). In this study, local MEs-coordinates are configured using four envelopes (see Figure 4e, Appendix B, and Figure B1d for the details on the coordinate transformation and the set-up), so that in the Nordic overflows region model levels are nearly terrain-following to a depth of 2,800 m.

Hereafter, the configurations using local vqs , szt , and MEs GVCs in the Nordic overflow region are simply referred to as GOSI- vqs , GOSI- szt , and GOSI-MEs configurations.

In order to reduce HPG errors, the envelope bathymetry surfaces of the GOSI- vqs and GOSI- szt configurations or the generalized envelopes of GOSI-MEs were smoothed using the iterative procedure detailed in Appendix C. Such a method uses the Martinho and Batteen (2006) smoothing algorithm to reduce the local slope parameter r

below multiple user defined r_{\max} values, effectively allowing one to apply distinct level of smoothing in different areas of the model domain. When using terrain-following computational levels, one of the main difficulties is defining an objective methodology to discern when HPG errors can be considered “acceptable” (e.g., Lemarié et al., 2012). In this study, we decided to apply increasingly more severe r_{\max} values only in those grid points where spurious currents were $\geq 0.05 \text{ m s}^{-1}$ (see Appendix C for the definition of the slope parameter and details on the actual r_{\max} values used in this work). Such a velocity threshold was chosen because it allowed us to significantly smooth the envelopes where HPG errors were large (i.e., spurious currents $\geq 0.01\text{--}0.02 \text{ m s}^{-1}$, the typical accuracy of moored velocity observations—see e.g., Daniault et al. (2016), McCarthy et al. (2020), and Johns et al. (2021)), while only marginally affecting areas involved with the overflows descent (see e.g., step 5 of Figure C1). Moreover, in the Denmark Strait overflow region, where HPG errors are expected to be large, typical current velocities are between 0.5 and 1 m s^{-1} (e.g., Jochumsen et al., 2015). Therefore, spurious currents $\leq 0.05 \text{ m s}^{-1}$ may be considered as acceptable in this region. While such a methodology allowed us to achieve a good compromise between reducing HPG errors and having model levels following the “true” topography in most of the grid points of the localization area, it is still somewhat arbitrary and more research might be needed to define a more general criterion.

Since szt -coordinates are nearly terrain-following only up to a certain prescribed depth, a more relaxed r_{\max} value can be potentially applied in comparison to a similar configuration using local vqs -levels, resulting in a less smoothed envelope bathymetry. This can allow one to keep HPG errors below an acceptable level while significantly reducing spurious “saw-tooth” structures in the model bathymetry. For this configuration, sensitivity tests (not presented in this work) showed that the $\approx 1,200 \text{ m}$ limit was the best compromise between reducing HPG errors and limiting the occurrence of spurious “saw-tooth” structures, while with a deeper limit the vqs and szt configurations would become inevitably very similar. A drawback of this choice is that when the Nordic overflows approach the deeper areas of the localized area, the benefits of using nearly terrain-following levels will not apply. Ezer (2005), Shapiro et al. (2013), and Bruciaferri et al. (2018, 2020) showed that models using geopotential coordinates represent significant larger mixing than models using terrain-following levels during the first stages of the dense water descent. Therefore, the szt configuration will inform us whether improving the representation of the initial cascade is sufficient for the continuation of a realistic dense plume.

The ME method allows for a 3D varying maximum slope parameter r_{\max} , effectively permitting to smooth the envelopes only where it is needed for maintaining HPG errors below an acceptable level. In such a way, the generation of undesired “saw-tooth” patterns and “step-like” structures can be significantly reduced in comparison to vqs and szt approaches. The ME approach offers great freedom in the configuration of the vertical grid, allowing one to directly control the design of model levels in each sub-zone of the vertical domain. However, such an increased flexibility results in a higher number of parameters to choose and tune in comparison to the vqs and szt approaches, making the mesh generation process more time-consuming.

4. Idealized Numerical Experiments

Two different types of idealized numerical experiments are conducted in this study. The first one assessed whether the localized terrain-following grids can accurately compute HPGs (Section 4.1), a basic requirement for a robust numerical mesh that will be used for realistic oceanic simulations. The second numerical experiment evaluates the ability of the various GVCs to reduce numerical diapycnal mixing when simulating overflows (Section 4.2).

4.1. Errors in the Computation of Pressure Forces

HPG errors affecting computational vertical grids are typically assessed via the classical HPG test of Haidvogel and Beckmann (1999). In this idealized numerical experiment, the ocean model is initialized at rest (i.e., $\mathbf{u} = 0$, $\eta = 0$) with a horizontally uniform stratification $\rho(z)$ so that initial horizontal density gradients are nil. In the absence of any external forcing and explicit tracers diffusion, the analytical solution for the ocean currents in this type of problem is 0 m s^{-1} . However, when using generalized $s(x, y, z, t)$ coordinates the horizontal pressure gradient $\nabla_z p$ (with $\nabla_z = (\partial_{x^1}, \partial_{y^1}, 0)$) becomes the result of two sizable terms

$$\nabla_z p = \nabla_s p + \rho g \nabla_s z. \quad (8)$$

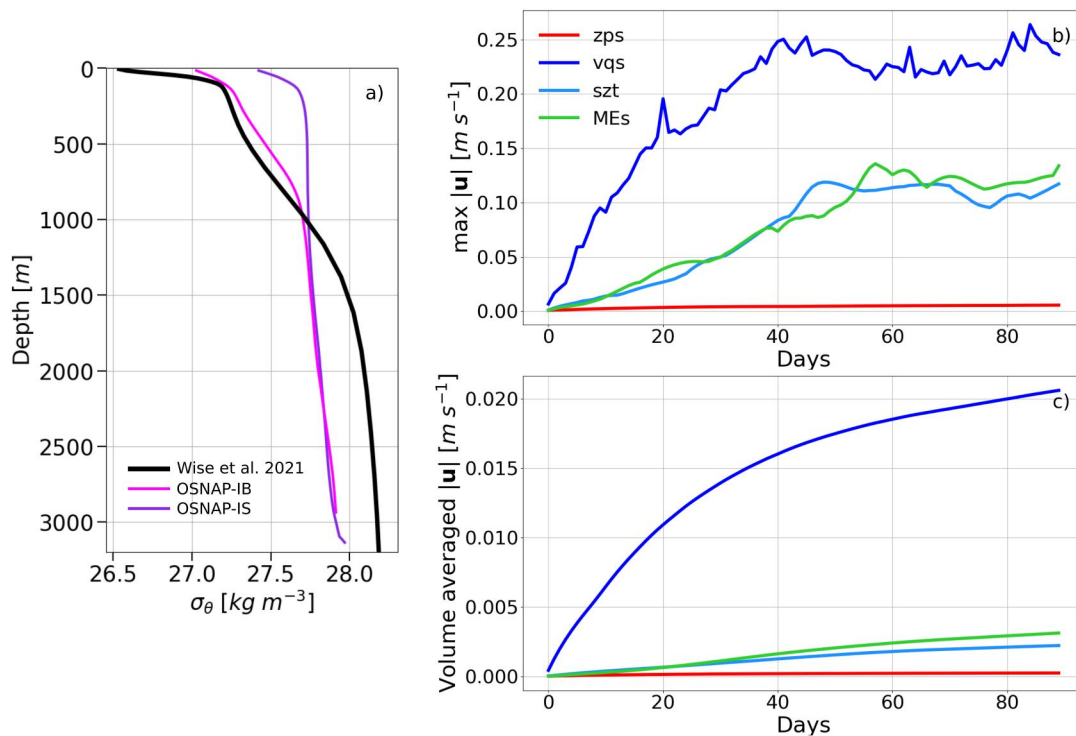


Figure 5. (a) Wise et al. (2021) synthetic σ_θ profile used to initialize HPG experiments and two observed σ_θ profiles extracted in the middle of the Irminger Sea (violet) and Icelandic Basin (magenta) legs of the OSNAP East array (see IS and IB sections in Figure 1). (b) Time evolution of the maximum velocity error for the GOSI- z^* ps (red), GOSI-vqs (blue), GOSI-szt (light blue) and GOSI-MEs (light green) configurations. (c) Same as (b) but for the mean velocity error (the average is calculated in the localization area, i.e., red and green areas in Figure 4a).

In the discrete limit, both terms on the right hand side of Equation 8 are affected by distinct numerical errors that generally do not cancel, generating spurious pressure forces that drive non-trivial unphysical currents (Ezer et al., 2002; Haney, 1991; Mellor et al., 1994).

Numerical errors in the computation of horizontal pressure forces depend both on the slope of the computational surfaces and the smoothness of the ambient stratification (e.g., Mellor et al., 1994). Hence, in order for a HPG test to be meaningful, the buoyancy profile used to initialize the experiment should be at least representative of the typical stratification present in the area of interest. A common practice is to choose an initial density profile that represents a more challenging buoyancy condition than the typical stratification, so that the robustness and accuracy of the model numerics could be tested under stress conditions. The control GOSI- z^* ps and the three GOSI-vqs, GOSI-szt, and GOSI-MEs global configurations are initialized with the synthetic buoyancy profile suggested by Wise et al. (2021). As shown in Figure 5a, such an initial density profile agrees well (especially in terms of vertical gradients) with observations from the Overturning in the Subpolar North Atlantic Program (OSNAP, M. S. Lozier et al. (2017, 2019)) East array in the upper 1,000 m and below 1,500 m (especially in the case of the Icelandic basin), while in the 1,000–1,500 m depth range represents a more challenging stratification in comparison to OSNAP measurements.

Numerical simulations were integrated for 90 days with no external forcing. Figure 5 presents the daily timeseries of the maximum (Figure 5b) and average (Figure 5c) spurious currents $|\mathbf{u}|$ for the four configurations. After ≈ 60 days, all the configurations present fully developed spurious currents where viscosity and friction balance the prognostic growth of the erroneous flow field (e.g., Berntsen, 2002; Berntsen et al., 2015; Mellor et al., 1998). GOSI- z^* ps shows the smallest HPG errors (both maximum and average spurious currents are $< 0.005 \text{ m s}^{-1}$, in agreement with previous studies, e.g., Bruciaferri et al., 2018; Wise et al., 2021). When using z -levels with partial steps, the near-bottom grid points within a vertical level are not necessarily at the same depth as the grid points in the interior, resulting in problems with pressure gradient errors and spurious diapycnal diffusion (Pacanowski et al., 1998), although much smaller than the ones affecting terrain-following models (Griffies, Böning, et al., 2000). The GOSI-vqs configuration presents the largest HPG errors—maximum and average spurious

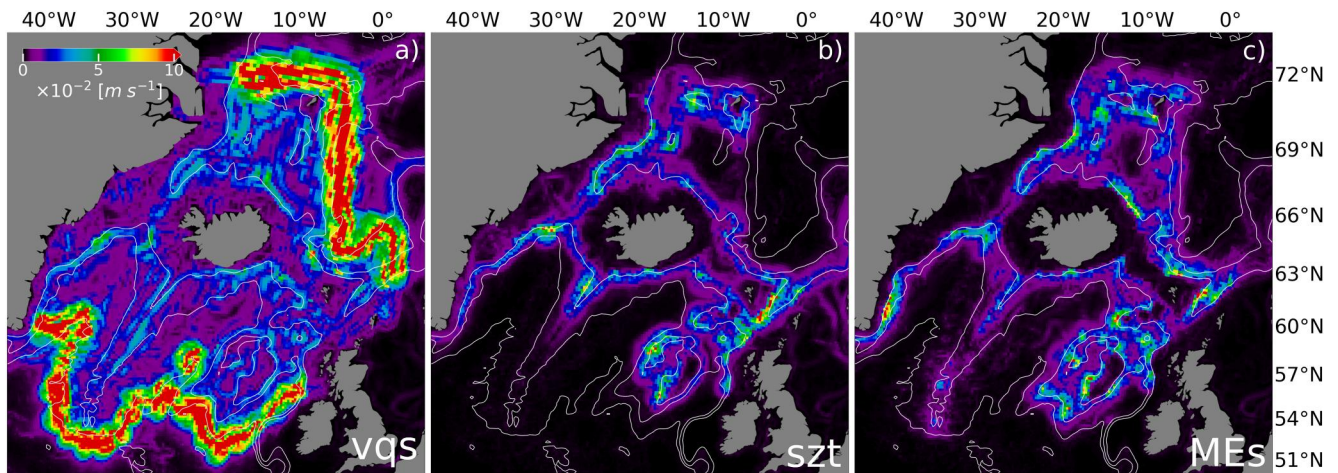


Figure 6. Maps of the maximum in the vertical and time spurious currents $lul\text{ m s}^{-1}$ after a 90 days long HPG numerical experiment for the models using localized vqs (a), szt (b) and MEs (c) GVC.

currents are >0.25 and $>0.02\text{ m s}^{-1}$, respectively. For both the GOSI-szt and GOSI-MEs configurations, the maximum and average spurious currents are ≈ 0.13 and $<0.005\text{ m s}^{-1}$, respectively. These results indicate that in the case of the GOSI-vqs configuration HPG errors affect a substantial part of the localization area while for the GOSI-szt and GOSI-MEs configurations spurious currents are significant only in few grid points of the model domain.

The envelopes of the three localized GVCs were computed using the same iterative algorithm with exactly the same smoothing parameters (see Section 3.2 and Appendix C for the details). In order to understand the reason why GOSI-vqs differs so significantly from the other two configurations, Figure 6 shows, for each grid point of the horizontal grid, the maximum velocity error lul in the vertical and in time for the three configurations using localized QE GVCs.

In the case of the GOSI-szt and GOSI-MEs configurations, HPG errors affect only the localization area (red area in Figure 4a), as expected. To the contrary, the vqs model presents large spurious currents in the proximity of the transition area (green region in Figure 4a). Since the local-vqs approach relies on one single envelope bathymetry, the mismatch in depth between vqs and z^* model levels sharing the same k index can be quite large ($\approx 3,500\text{ m}$ in the case of the last model level), resulting in two important consequences for the transition zone (see Figures 4c and B1b). First, computational surfaces will be particularly steep in the transition area, driving large HPG errors that can not be mitigated by limiting the slope parameter of the envelope bathymetry. Second, significant “saw-tooth” patterns will be generated in the model bathymetry of the transition zone, introducing unrealistic spurious noise at the model grid scale (see Figure 4c, beyond 1,500 km, and Figure B1b before 800 km and beyond 1,500 km). In agreement with Colombo (2018), we note that while the large HPG errors could be reduced by implementing a much wider transition area, the generation of undesired bathymetric noise in the relaxation zone appears to be a much harder problem to solve.

Neither the GOSI-szt nor GOSI-MEs configurations suffers from the same issues affecting local-vqs coordinates. For example, because at depth the szt approach uses the same vertical coordinate formulation of the global domain, the GOSI-szt bathymetry in the transition zone is effectively discretized with z^* ps levels (see Figures 4d and B1c), resulting in a smooth transition zone. Similarly, since the ME approach divides the model vertical space in sub-zones, model levels can be easily distributed along the water column to obtain a smooth transition zone with very small HPG errors (see Figures 4e and B1d and Appendix B). Given the large HPG errors affecting the GOSI-vqs configuration (average spurious currents are $\geq 0.02\text{ m s}^{-1}$, the upper limit of the typical accuracy range of moored velocity observations, e.g., Daniault et al., 2016; Johns et al., 2021; McCarthy et al., 2020), we conclude that the vqs approach is not suitable for the localization method proposed in this manuscript and we continue our study only with the GOSI-szt and GOSI-MEs models.

In the case of the GOSI-szt and GOSI-MEs configurations, the numerical tests of this section have shown that the algorithm described in Appendix C can be successfully used to significantly reduce the average spurious currents

(<0.005 m s⁻¹, the same order of the spurious currents affecting GOSI-z*ps). However, it also showed that their maximum spurious currents are still large (>0.10 m s⁻¹). We think that the main problem was the length of the HPG tests used to identify where to smooth the envelopes (see Appendix C). One month was not long enough for the spurious currents to fully develop everywhere in the domain, preventing the iterative algorithm from identifying all the problematic grid points where smoothing was needed. This can be easily seen in the case of the GOSI-MEs configuration: in the 90 days long HPG experiment, spurious currents ≥0.10 m s⁻¹ affect few grid cells along the continental slope of Greenland (1,000–1,500 m) just before Cape Farewell (see Figure 6c) while they are not present in the 1 month long HPG test (see step 4 of Figure C1). Therefore, future applications of the iterative smoothing algorithm should first assess the minimum length needed by a HPG test to have fully developed spurious currents.

Finally, we note that this idealized set of experiments is also interesting because highlights a possible limitation of our localization method: it can be successfully applied only if at least one of the two coordinate systems at stake is flexible enough to allow a smooth transition between the two, as in the case of the *szt* and MEs GVCs. We believe this was probably also one of the main reasons behind the issues experienced by Colombo (2018), since their approach targeted the “not-so-adaptable” *vqs* coordinates.

4.2. Diapycnal Mixing in an Idealized Overflow

Models with a stepped bottom topography introduce excessive numerical mixing when simulating dense gravity currents. This is the case especially at coarse horizontal resolutions such as the one used in this study, even when the partial steps parameterization is employed (e.g., Legg et al., 2006). Contrarily, terrain-following levels can offer a smooth representation of the sea bed, facilitating more realistic simulations of bottom intensified currents (e.g., Ezer & Mellor, 2004). The aim of this second set of idealized experiments is to evaluate the ability of localized GVCs to reduce spurious entrainment and diapycnal mixing when simulating gravity currents generated by a dam-break in the Denmark Strait.

Numerical experiments are set as follows. The original model bathymetry is modified by introducing an artificial reservoir in the proximity of the Denmark Strait sill, as shown in Figure 7a. Then, the model uses a linear equation of state (only function of temperature) and is initialized with a horizontally uniform ambient stratification $\rho(z)$ that linearly fits the observed density distribution in the middle of the Irminger Sea, as shown in Figure 7b—observations are from the OSNAP array (M. S. Lozier et al., 2017, 2019). Such an initial condition is perturbed by introducing a cold dense water mass with density ρ_d inside the artificial reservoir which extends through the entire water column and such that $\Delta\rho = \max\{\rho_d - \rho(z)\} = 1.3 \text{ kg m}^{-3}$. As already noted by Ezer (2006), this value for $\Delta\rho$ is somewhat larger than the ones observed in reality. However, one has to keep in mind that our simulations are lock-exchange gravity currents where the only forcing is represented by the buoyancy anomaly of the dense perturbation in the artificial reservoir. Therefore, $\Delta\rho$ needs to be large enough to promote a down-slope dense cascade that will continue even after the inevitably strong mixing at the beginning of the simulation. We emphasize that the aim of this second idealized experiment is to evaluate the impact of the vertical coordinate system on the simulation of a gravity current in the Denmark Strait, and not to reproduce observed properties of the overflow in this region.

In order to keep track of the cascading dense plume and facilitate our analysis, we use a passive tracer whose initial concentration C is 10 in the cold dense water mass of the artificial reservoir while zero elsewhere. Computations are integrated for 90 days without any external forcing and using the standard GOSI-025 setting for the numerics and the physics (Section 3.1), except for the use of the linear equation of state. In particular, ambient fluid entrainment and vertical mixing are explicitly taken into account by using the standard NEMO turbulent kinetic energy (TKE) scheme (see Storkey et al. (2018) for the details).

Dilution of the tracer concentration C is an indication for entrainment and mixing in of ambient fluid in the dense cascading water (Ezer, 2005; Legg et al., 2006). We define the overflow water to be the fluid with $C \geq 0.1$ and Figures 8 and 9 show snapshots of the tracer concentration at the deepest wet cell just above the bottom topography (top row) and in a vertical cross section along the plume path (bottom row) for the three configurations after 30 and 90 days, respectively. All the three configurations simulate a dense water plume descending down the steep continental slope of the northern Irminger Sea basin which reaches the 2,800 m after 90 days. However, their respective solutions for the passive tracer concentration distribution differ significantly.

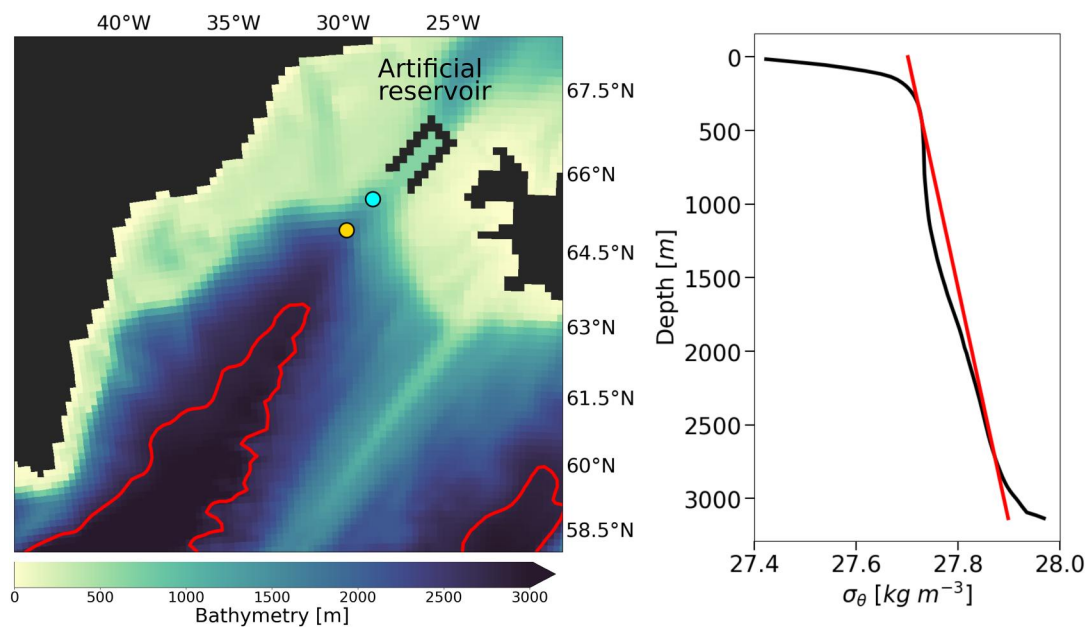


Figure 7. (a) In the idealized overflow experiment, the original model bottom topography is modified to include an artificial reservoir in the proximity of the Denmark Strait. In red it is also shown the 2,800 m isobath defining the boundary of the localization area. The yellow and cyan dots present the location where the velocity profiles shown in panels (a) and (b) of Figure 10, respectively, are extracted. (b) Density vertical profile from OSNAP observational array in the Irminger Sea (black) compared against the analytical density profile (red) used to initialize the idealized overflows experiments.

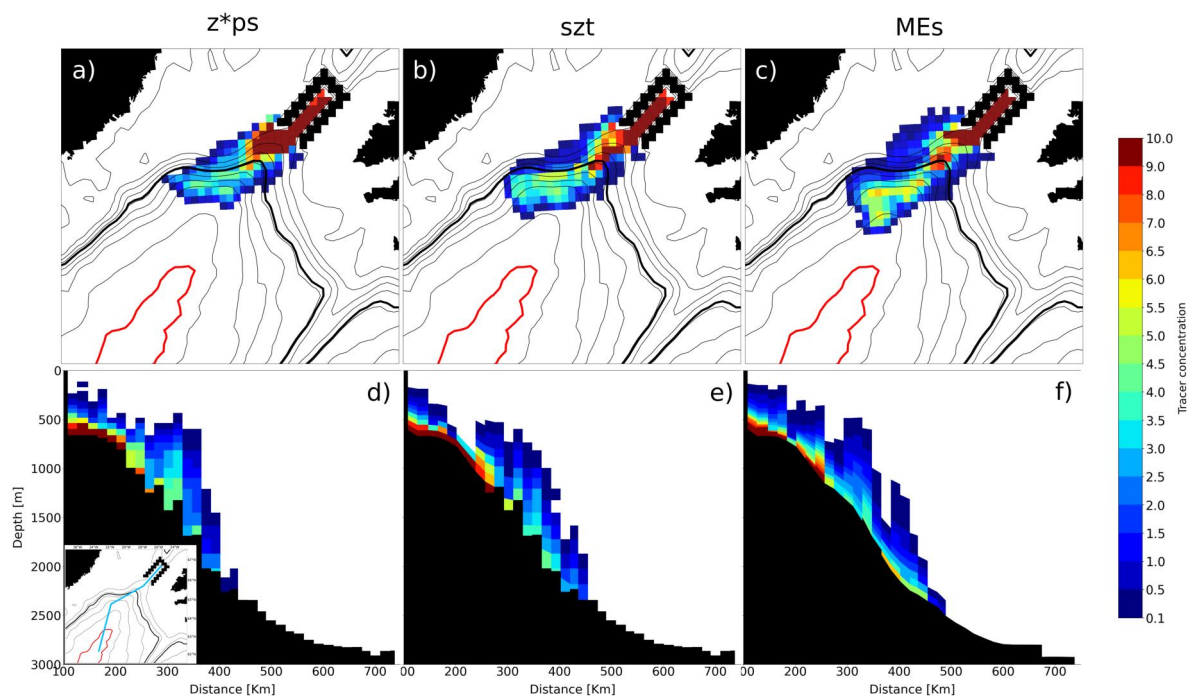


Figure 8. Passive tracer concentration at the bottom (upper row) and in a cross section passing through the dense plume (bottom row) for the GOSI-z*ps, GOSI-szt, and GOSI-MEs configurations after 30 days. Only wet cells with passive tracer concentration $C \geq 0.1$ are shown. The location of the cross section is shown in light blue in the inset. The thick red and black lines identify the 2,800 and 1,200 m isobaths, respectively.

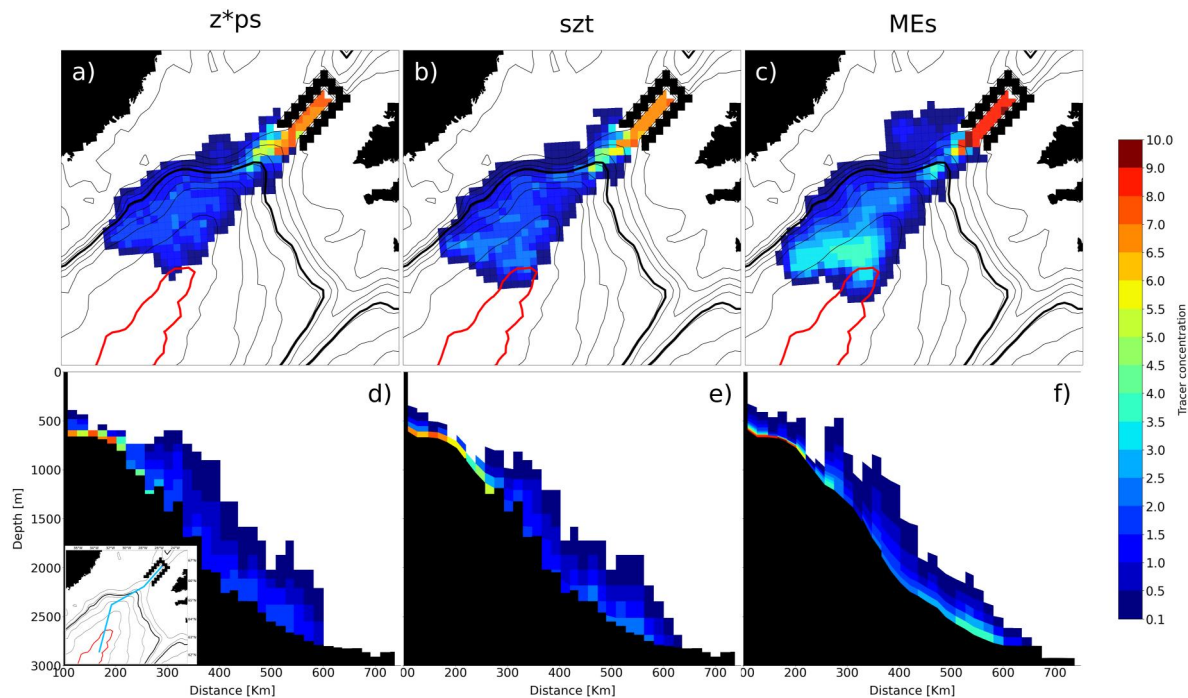


Figure 9. Same as Figure 8 but after 90 days.

The control GOSI- z^*ps configuration produces the most diluted overflow (Figures 8a, 8d, 9a, and 9d), indicating large ambient fluid entrainment and mixing, in agreement with previous studies (e.g., Bruciaferri et al., 2018; Ezer, 2005). In the case of the GOSI-MEs configuration, diapycnal mixing is significantly reduced, allowing the simulation of a much less diluted dense plume which after 90 days can reach the 2,800 m isobath with up to 45% of the initial passive tracer concentration (see Figures 9c and 9f). The GOSI- sz_t configuration is able to reduce the large mixing in the first third of the simulation, reproducing a passive tracer concentration distribution similar to the one of GOSI-MEs (Figures 8b and 8e). However, the relatively shallow (1,200 m) transition to a stepped topography leads to an increase in diapycnal mixing in the last two thirds of the simulation, slowing down and importantly diluting the GOSI- sz_t overflow (Figures 9b and 9e).

Qualitative examination of Figure 8 seems to suggest that the three configurations may also differ in the way they represent the evolving dynamics of the dense plume. At the beginning of the simulation, the three configurations agree in simulating a coherent down-slope cascading. However, after crossing the $\approx 1,000$ m isobath, the overflow reproduced by GOSI- z^*ps and GOSI- sz_t seem to move prevalently in the along-slope direction, with the bulk of the dense plume reaching a depth of $\approx 2,000$ m after 30 days (see Figures 8a and 8b). In the case of GOSI-MEs, after 30 days the head of the dense plume has crossed the 2,500 m, indicating a larger down-slope component of the velocity. As demonstrated by Figure 10, this is due to the fact that GOSI-MEs, with its increased resolution near the sea bed, is able to better resolve the Ekman transport at the bottom boundary layer. From scaling arguments, the Ekman-layer thickness h_E can be estimated using the relation $h_E = \kappa u^* f^{-1}$, where $\kappa = 0.41$ is the von Karman constant, f is the Coriolis parameter and u^* is the friction velocity (Cushman-Roisin & Beckers, 2011). Considering an idealized overflow with a speed of $\approx 0.3 \text{ m s}^{-1}$ and computing u^* via a quadratic bottom friction formulation with a drag coefficient C_D of 3×10^{-3} , the bottom Ekman depth is ≈ 50 m. In the initial depth range of the overflow (between ≈ 600 and 1,500 m), the GOSI-MEs configuration has a bottom resolution between ≈ 10 and 20 m, while in the case of the GOSI- z^*ps and GOSI- sz_t configurations the bottom resolution is >50 m. Therefore, the GOSI-MEs configuration is able to partially resolve the bottom Ekman layer while the GOSI- z^*ps and GOSI- sz_t are not. These results are in agreement with the findings of Ezer (2005) for the case of a classic terrain-following σ -model or the study of Colombo et al. (2020) which employed z^*ps -based models with very high vertical resolution (150 and 300 number of levels).

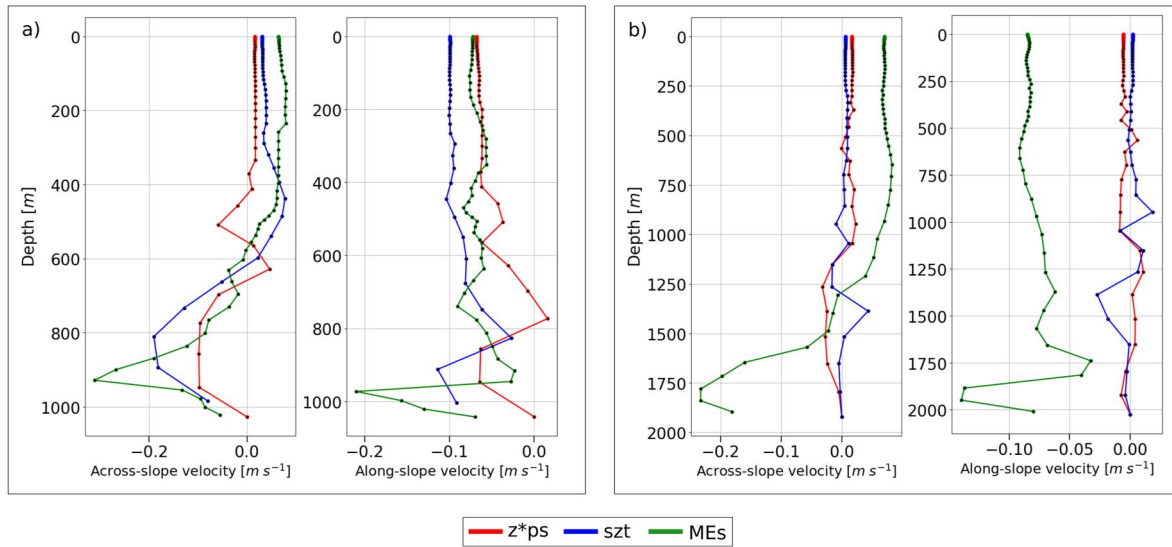


Figure 10. Cross- and along-slope velocity components profiles (hourly mean) for GOSI- z^*ps (red), GOSI- szt (blue) and GOSI-MEs (green) configurations after 7 (panel a) and 15 (panel b) days.

To evaluate and compare diapycnal mixing in our three simulations, Figure 11 presents the time evolution of the distribution in density space of the total amount of passive tracer mass $Tr(x, y, \sigma_\theta, t)$. Computations are carried out for 21 density classes ($\Delta\sigma_\theta = 0.06 \text{ kg m}^{-3}$) and time windows Δt of 4 days. Such a metric is a modified version of the diagnostic first proposed by Ezer (2005) and Legg et al. (2006). At the beginning of the experiments, the passive tracer marks only the heaviest density class, as in the initial condition. Once the dense overflow is initiated, all the three configurations reproduce strong diapycnal mixing and entrainment in the first ≈ 20 – 30 days of the simulations, with the majority of the passive tracer moving toward lighter density classes. In the case of GOSI- z^*ps and GOSI- szt , the passive tracer lands and marks for the remaining two thirds of the simulations few (≈ 2 – 3) of the lightest density classes. To the contrary, in the GOSI-MEs case after 30 days and in the second part of the simulation the passive tracer is spread within a larger number of relatively heavier density classes, demonstrating reduced diapycnal mixing.

Both GOSI- z^*ps and GOSI- szt configurations present also a secondary constant diapycnal passive tracer transport event that starts around day 40 and continues until the end of the experiments and that is not present in the GOSI-MEs simulation. Figure 8 suggests that this is probably due to a larger volume of source dense water that is not able to cascade down the continental slope in the case of GOSI- z^*ps and GOSI- szt and slowly mixes with the surrounding ambient water.

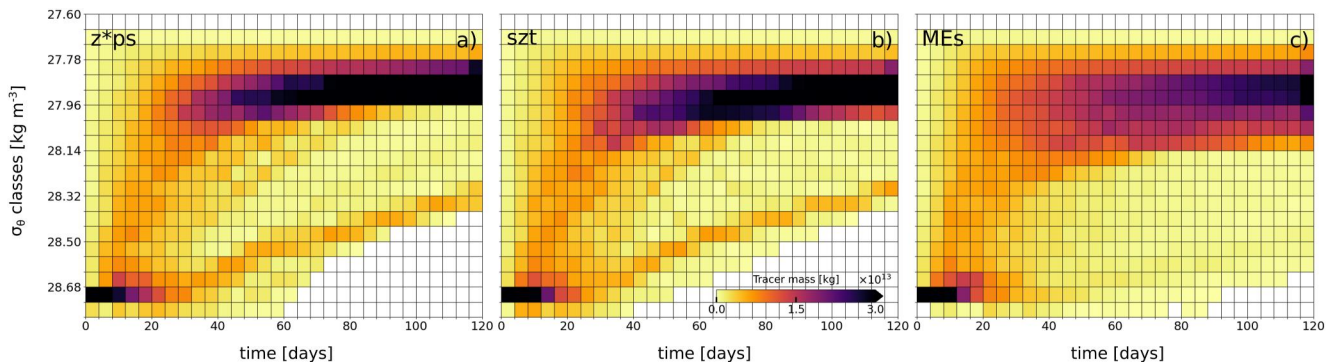


Figure 11. Distribution in density space and time of the total amount of passive tracer mass $Tr(x, y, \sigma_\theta, t)$ in kg for 21 density classes ($\Delta\sigma_\theta = 0.06 \text{ kg m}^{-3}$) and time windows Δt of 4 days for the GOSI- z^*ps (a), GOSI- szt (b) and GOSI-MEs (c) models.

Table 1
List of Observational Data Sets Used to Analyze the Results of the Realistic Experiments

ID	Covered geographical area	Variables	Validity period	Data set type	References
WOA18	World Ocean	Bottom Tem. and Sal.	2005–2017	Clim. field @ 1/4° hor. res.	Boyer et al. (2018)
DS	Denmark Strait	Tem., Sal.	1990–2012	Clim. section	Mastropole et al. (2017)
		OVF vol. transp.	1996–2015	Average value	Østerhus et al. (2019)
IS	Irminger Sea	Tem., Sal., Vel.	2014–2018	30 days mean sections	M. S. Lozier et al. (2017) and Li et al. (2023)
IB	Icelandic basin	Tem., Sal., Vel.	2014–2018	30 days mean sections	M. S. Lozier et al. (2017) and Li et al. (2023)
IFR	Iceland-Faroe Ridge	Tem., Sal.	August 2016	Mean section	Quadfasel (2018) and Hansen et al. (2018)
FSC	Faroe-Shetland Channel	Tem., Sal.	1994–2005	Clim. section	Hansen and Østerhus (2000) and Hughes et al. (2006)
FBC	Faroe-Bank Channel	OVF vol. transp.	1994–2005	Average value	Østerhus et al. (2019)
WTR	Wyville Thomson Ridge	OVF vol. transp.	2006–2013	Average value	Østerhus et al. (2019)
CFGZ	Charlie-Gibbs Fracture Zone	OVF vol. transp.	2010–2012	Average value	Xu et al. (2018)

5. Realistic Integrations

In the last set of numerical experiments the skills of the GOSI- z^* ps, GOSI- sz t, and GOSI-MEs configurations in reproducing observed properties of the Nordic overflows are assessed. Numerical simulations are initialized with EN4 1995–2014 climatological January data (Good et al., 2013) and integrated from 01-01-2010 to 01-01-2019 using the setting for the forcing, numerics and physics described in Section 3.1. The first 4 years of the computations are considered spin-up time and numerical results are analyzed for the period 2014–2018.

5.1. Observations and Analysis Methodology

Numerical results are analyzed and compared to observations in terms of hydrographic properties and total volume transports of the Nordic overflows. Observations include the World Ocean Atlas 2018 objectively analyzed climatology (WOA18; Boyer et al., 2018) for the bottom temperature and salinity as well as a number of selected cross-sections of measured in situ temperature, salinity and normal velocities—see Table 1 for the details and Figure 1 for the geographical location of the sections. In the case velocities observations were not available for a particular section, previously published estimates of overflows volume transport are used instead.

The positive northward volume transport in Sv ($1 \text{ Sv} = 10^6 \text{ m}^3 \text{ s}^{-1}$) of the observed (when available) and simulated dense overflows $\Psi^*(\tilde{\sigma}_\theta, t)$ is calculated as

$$\Psi^*(\tilde{\sigma}_\theta, t) = \iint_{A^*} \mathbf{u} \cdot \hat{\mathbf{n}} \, dA, \quad (9)$$

where $\mathbf{u}(x, y, z, t)$ is the horizontal velocity field, $\hat{\mathbf{n}}$ is a unit vector normal to the cross section and A^* represents the area of the cross section where the potential density anomaly σ_θ is larger than a chosen $\tilde{\sigma}_\theta$ threshold.

Similarly, the mean hydrographic properties of overflows water masses are computed as

$$\phi^*(\tilde{\sigma}_\theta, t) = \frac{1}{V^*} \iiint_{V^*} \phi \, dV, \quad (10)$$

where $\phi(x, y, z, t)$ can be either temperature (T), salinity (S) or potential density anomaly (σ_θ) and V^* is the volume of water with $\sigma_\theta \geq \tilde{\sigma}_\theta$.

Typically, a widely accepted value of $\tilde{\sigma}_\theta = 27.80 \text{ kg m}^{-3}$ is used to separate the Nordic overflows water masses from the surrounding ambient fluid in the proximity of the Greenland-Scotland ridge (e.g., Dickson & Brown 1994; Østerhus et al., 2019). As we will show later in our analysis (see Section 5.2), such a value for $\tilde{\sigma}_\theta$ works well also in our simulations to identify the dense waters of the overflows upstream.

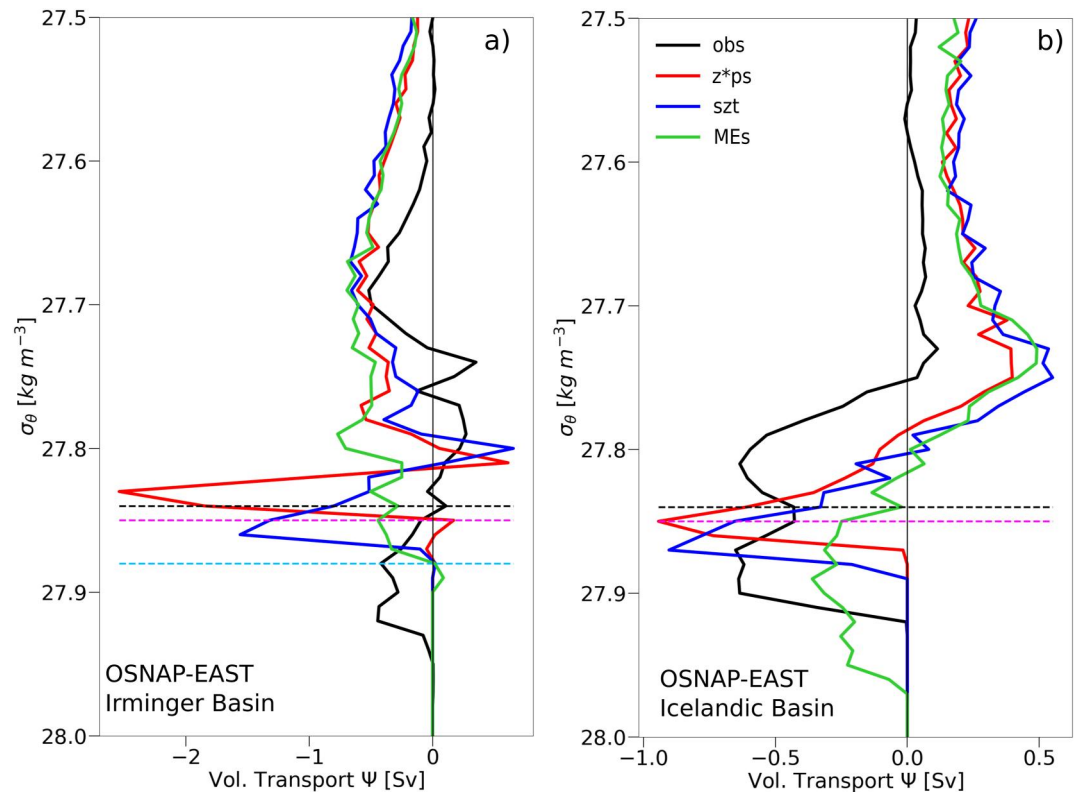


Figure 12. Volume transports (positive northward) integrated in potential density bins of 0.01 kg m^{-3} and averaged across the 2014–2018 period for OSNAP observations (in black) and GOSI- z^*ps (red), GOSI- szt (blue) and GOSI-MEs (green) configurations in the Irminger Sea (a) and in the Icelandic basin (b). The black dashed lines mark the $\bar{\sigma}_\theta = 27.84 \text{ kg m}^{-3}$ limit adopted in this study to identify overflow waters. The magenta and light blue dashed lines represent the limits ($\bar{\sigma}_\theta = 27.85 \text{ kg m}^{-3}$ and $\bar{\sigma}_\theta = 27.88 \text{ kg m}^{-3}$, respectively) typically used in literature to define DSOW and ISOW water masses downstream.

Because of the entrainment of generally saltier ambient waters, a larger value for $\bar{\sigma}_\theta$ is usually applied in the literature to track the modified DSOW and ISOW water masses farther downstream. Typical values are $\bar{\sigma}_\theta = 27.85 \text{ kg m}^{-3}$ (Dickson et al., 2008) or $\bar{\sigma}_\theta = 27.88 \text{ kg m}^{-3}$ (Kieke & Rhein, 2006) in the case of DSOW and $\bar{\sigma}_\theta = 27.85 \text{ kg m}^{-3}$ for the ISOW (e.g., Holliday et al., 2015; Xu et al., 2010). However, as we will show later (see Section 5.3), excessive spurious mixing affects the GOSI- z^*ps and GOSI- szt configurations, preventing them from representing such dense waters in the deep Irminger and Icelandic basins.

Therefore, a different threshold is needed in order to identify overflows waters downstream the Greenland-Scotland ridge in our simulations. Ideally, the $\bar{\sigma}_\theta$ cutoff should be the boundary that separates the densest water masses in the basin where a local maximum in volume transport exists. A value of $\bar{\sigma}_\theta = 27.84 \text{ kg m}^{-3}$ is chosen in this work. As shown later in Section 5.3, such a limit identifies in the IS and IB cross-sections dense water masses that agree well for both observations and modeling results. In addition, Figure 12 presents the 2014–2018 mean volume transports distribution as a function of potential density classes. In the case of the ISOW (Figure 12b), the $\bar{\sigma}_\theta = 27.84 \text{ kg m}^{-3}$ limit correctly identifies the densest water masses in the observations and the models with a relative peak in the volume transports. For the DSOW (Figure 12a), the chosen threshold works well for the observations and the GOSI- szt and GOSI-MEs configurations, while it does not capture the densest local maximum in transport for the case of the GOSI- z^*ps configuration. However, we note that the relative peak of GOSI- z^*ps is only marginally missed, while using a lower $\bar{\sigma}_\theta$ limit will inevitably include in the analysis of the observations lighter waters not belonging to the overflows.

Table 2
Time Averaged (Mean \pm SD) Temperature ($\langle T^* \rangle$), Salinity ($\langle S^* \rangle$), Potential Density Anomaly ($\langle \sigma_{\theta}^* \rangle$) and Transport ($\langle \Psi^* \rangle$) of Overflow Water Masses ($\bar{\sigma}_{\theta} = 27.80 \text{ kg m}^{-3}$) Estimated From Observations and Simulated by the Models in the DS, FSC, IFR, FBC, and WTR Upstream Sections

Section ID	Variables	Observations	GOSI-z*ps	GOSI-szt	GOSI-MEs
DS	$\langle T^* \rangle$ ($^{\circ}\text{C}$)	0.74	1.96 ± 0.49	2.22 ± 0.48	1.99 ± 0.49
	$\langle S^* \rangle$	34.85	34.96 ± 0.04	34.98 ± 0.05	34.97 ± 0.05
	$\langle \sigma_{\theta}^* \rangle$ (kg m^{-3})	27.94	27.93 ± 0.01	27.93 ± 0.01	27.94 ± 0.01
	$\langle \Psi^* \rangle$ (Sv)	-3.2 ± 0.5	-2.2 ± 0.4	-2.0 ± 0.3	-2.3 ± 0.4
IFR	$\langle T^* \rangle$ ($^{\circ}\text{C}$)	2.52	2.63 ± 0.39	2.93 ± 0.49	2.64 ± 0.40
	$\langle S^* \rangle$	34.97	34.97 ± 0.03	34.99 ± 0.04	34.97 ± 0.03
	$\langle \sigma_{\theta}^* \rangle$ (kg m^{-3})	27.90	27.89 ± 0.02	27.88 ± 0.01	27.89 ± 0.02
	$\langle \Psi^* \rangle$ (Sv)	-0.4 ± 0.3	-2.2 ± 0.4	-2.0 ± 0.3	-0.3 ± 0.2
FSC	$\langle T^* \rangle$ ($^{\circ}\text{C}$)	0.67	0.49 ± 0.16	1.44 ± 0.19	0.79 ± 0.23
	$\langle S^* \rangle$	34.92	34.93 ± 0.01	34.98 ± 0.02	34.94 ± 0.01
	$\langle \sigma_{\theta}^* \rangle$ (kg m^{-3})	27.99	28.01 ± 0.01	27.98 ± 0.01	27.99 ± 0.01
FBC	$\langle \Psi^* \rangle$ (Sv)	-2.0 ± 0.3	-2.0 ± 0.3	-2.0 ± 0.4	-2.0 ± 0.4
WTR	$\langle \Psi^* \rangle$ (Sv)	-0.2 ± 0.1	0.0 ± 0.0	-0.2 ± 0.3	-0.1 ± 0.1

5.2. Properties of the Nordic Overflows Entering the North Atlantic

We begin our analysis evaluating the characteristics of the overflows simulated by the three configurations when crossing the Greenland-Scotland ridge. Table 2 compares the 2014–2018 time-averaged values of the overflows mean hydrographic properties simulated by the three configurations in the proximity of the upstream DS, IFR, and FSC cross-sections and the mean volume transports reproduced in the DS, IFR, FBC, and WTR sections (see Table 1 for more details, Figure 1 for the locations of the sections and Appendix D for a list of the acronyms) against existing estimates from observations (the actual time-series used to compute the time averages can be found in Figures S1 and S2 of the Supporting Information S1). In addition, Figure 13 compares the 2014–2018 averaged potential density, temperature and salinity fields simulated by the three configurations in the DS, IFR, and FSC cross-sections against the observations. As explained in Section 5.1, in the proximity of the Greenland-Scotland ridge the Nordic overflows water masses are identified using the threshold $\bar{\sigma}_{\theta} = 27.80 \text{ kg m}^{-3}$.

In the case of the DS section, the three configurations simulate density structures which are very similar and in agreement with the observations (see Figures 13a.1–13d.1 and Table 2). However, the analysis of the temperature and salinity fields indicate that large biases consistently affect the DSOW represented by the three configurations (see Figures 13a.2–13d.2 and 13a.3–13d.3 and Table 2), with mean salinity errors >0.1 and average warm biases $>1.0^{\circ}\text{C}$. The three configurations also underestimate the DSOW mean volume transport in the DS section (differences are $\approx 1 \text{ Sv}$, see Table 2).

In the proximity of the IFR section, the GOSI-z*ps and GOSI-MEs configurations simulate ISOW with mean hydrographic properties very similar to the observations (warm bias of $\approx 0.1^{\circ}\text{C}$ and average absolute salinity errors <0.01), resulting in marginally less dense ($\approx 0.01 \text{ kg m}^{-3}$) overflows water masses (see Figures 13e.*–13h.* and Table 2). In the case of GOSI-szt, results present moderately larger errors, with average values of $\approx 0.5^{\circ}\text{C}$ for temperature, ≈ 0.025 for salinity and $\approx 0.02 \text{ kg m}^{-3}$ for density. For the mean volume transport (see Table 2), GOSI-MEs results to be the more accurate (errors $<1.0 \text{ Sv}$) while GOSI-z*ps and GOSI-szt configurations present larger biases ($>1.5 \text{ Sv}$).

In the case of the FSC section, only climatological hydrographic observations from Hansen and Østerhus (2000) and Hughes et al. (2006) were accessible in this study, while direct estimations of the overflows volume transport were available only for the two farthest downstream FBC and WTR sections. In the FSC section, GOSI-szt simulates an ISOW that is moderately warmer and saltier than the observations (mean absolute errors of $\approx 0.7^{\circ}\text{C}$ and ≈ 0.06 , respectively), while the GOSI-z*ps and GOSI-MEs show much reduced biases (mean absolute errors $<0.2^{\circ}\text{C}$ for temperature and ≤ 0.02 for salinity, see also Figures 13i.*–13l.* and Table 2). For the volume transport (see Table 2), the three configurations are in good agreement with the observations in the case of the FBC section;

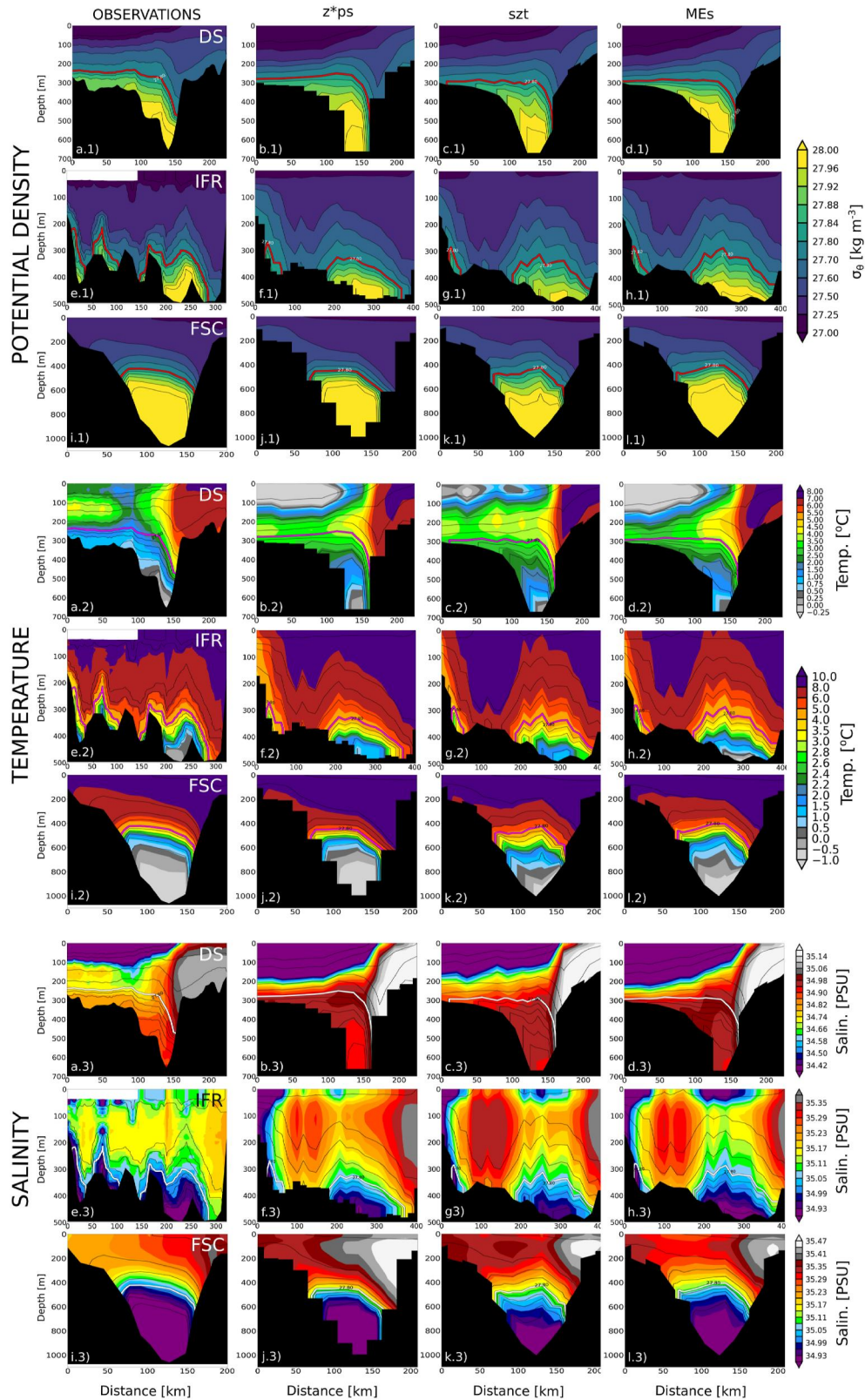


Figure 13. Potential density anomaly (panels *a.1–l.1*), temperature (panels *a.2–l.2*) and salinity (panels *a.3–l.3*) fields observed (1st column) and simulated by the GOSI- z^*ps (2nd column), GOSI- szt (3rd column) and GOSI-MEs (4th column) configurations in the Denmark Strait (DS), Iceland-Faroe-Ridge (IFR) and Faroe-Bank-Channel (FBC) cross-sections (see Table 1). The red, magenta and white lines show the 28.80 kg m^{-3} isopycnal.

in the WTR transect, GOSI-*szt* presents the highest accuracy while GOSI-MEs shows large differences with the observations and the GOSI-*z*ps* configuration totally misses this secondary path of the Nordic overflows. However, Figure S2 in Supporting Information S1 shows that in the case of the GOSI-*z*ps* and GOSI-MEs configurations the transport across the WTR section is very sporadic. Interestingly, this result seems to hold also with different overflow definitions, suggesting that this secondary path of the Nordic overflows might not be well represented in all the three configurations.

There are two key points to draw from this Section. First, we note that similar biases in temperature, salinity and transport seem to affect the three configurations, with larger magnitude in the Greenland-Iceland ridge (i.e., the DS section) than in the Iceland-Scotland ridge (i.e., the FSC, FBC, IFR, and WTR sections). Second, we observe that in general the local MEs GVC seems to have a small positive impact on the mean properties of the overflows upstream, while using local *szt* levels seems to somewhat degrade the properties of the simulated DSOW and ISOW, especially in the case of the FSC and IFR sections.

5.3. Dense Overflows Downstream the Greenland-Scotland Ridge

We continue our analysis assessing the properties of the Nordic overflows simulated by the three configurations downstream the Greenland-Scotland ridge. Table 3 compares the 2014–2018 time-averaged values of measured and simulated mean overflows hydrographic properties in the IS and IB sections and the overflows volume transport in the IS, IB, and CGFZ sections (see Table 1 for more details and Figures S3 and S4 of the Supporting Information S1 for the actual time-series). Moreover, Figure 14 presents the 2014–2018 averaged potential density anomaly, temperature and salinity fields observed and simulated by the three configurations along the OSNAP East array (Li et al., 2023; M. S. Lozier et al., 2017), which includes the Irminger Sea (IS) and the Icelandic Basin (IB) sections. Downstream the Greenland-Scotland ridge we use a density threshold $\bar{\sigma}_\theta$ of 27.84 kg m⁻³ to identify the modified DSOW and ISOW water masses (see Section 5.1 for the details).

In the IS section, GOSI-MEs is able to reproduce a modified overflow water mass which is in good agreement with the observations for the density (mean absolute error is <0.003 kg m⁻³). Contrarily, in the case of the GOSI-*z*ps* and GOSI-*szt* simulations the deep waters are less dense than measurements, with an average absolute bias >0.01 kg m⁻³ (see upper rows of Figure 14 and Table 3). Our analysis also shows that important positive biases in temperature (>0.3°C) and salinity (>0.01) affect the three configurations (see middle and bottom rows of Figure 14 and Table 3). In the case of the transport, the 2014–2018 mean DSOW volume transport simulated by GOSI-MEs is the most similar to the one estimated from OSNAP observations, followed by the ones of GOSI-*szt* and GOSI-*z*ps*.

The results for the overflow density in the IB section are similar to the ones of the IS section, with the GOSI-MEs configuration being the only one able to reproduce deep dense water masses with $\sigma_\theta > 27.88$ kg m⁻³ as the observations (see upper rows of Figure 14 and Table 3). In addition, all three configurations present a mean positive bias >0.01 for the overflow salinity in the IB section (see bottom rows of Figure 14 and Table 3); for the temperature (see middle rows of Figure 14 and Table 3) the GOSI-*z*ps* and GOSI-*szt* simulations show warm biases of ≈ 0.4 and ≈ 0.3 °C, respectively, while the GOSI-MEs configuration is in very good agreement with the observations (mean absolute bias ≈ 0.05 °C). Regarding the volume transport, the mean estimate from the GOSI-MEs simulation is the closest to observations (difference is <2 Sv), while GOSI-*z*ps* and GOSI-*szt* mean values present larger biases (see Table 3).

In the case of CGFZ section, no hydrographic observations were available for this study and the mean volume transport estimate of Xu et al. (2018) is used. For the GOSI-*z*ps* configuration, a small mean transport in the opposite direction of the observations exists (see Table 3), while the GOSI-*szt* simulation reproduces a mean transport that agrees with the observations in direction but is significantly weaker. In contrast, the GOSI-MEs configuration represents a northward volume transport that better agrees with published estimates of magnitude (see Table 3).

In agreement with the findings of the idealized overflow experiment of Section 4.2, this Section demonstrates that the type of vertical coordinates has a large impact on the accuracy of the simulated overflows downstream the Greenland-Scotland ridge. Using local ME terrain-following levels seems to allow the model to quickly improve the large inaccuracies of the initial condition at depth (see Figure S3 in Supporting Information S1 for more details) and reproduce deep overflow water masses that are similar in density to the observations. Conversely,

Table 3

Time Averaged (Mean \pm SD) Temperature ($\langle T^* \rangle$), Salinity ($\langle S^* \rangle$), Potential Density Anomaly ($\langle \sigma_\theta^* \rangle$) and Transport ($\langle \Psi^* \rangle$) of Overflow Water Masses ($\bar{\sigma}_\theta = 27.84 \text{ kg m}^{-3}$) Estimated From Observations and Simulated by the Models in the IS, IB, and CGFZ Downstream Sections

Section ID	Variables	Observations	GOSI-z*ps	GOSI-szt	GOSI-MEs
IS	$\langle T^* \rangle$ ($^{\circ}\text{C}$)	2.52 ± 0.02	2.83 ± 0.03	2.93 ± 0.01	2.82 ± 0.01
	$\langle S^* \rangle$	34.93 ± 0.00	34.94 ± 0.00	34.95 ± 0.00	34.96 ± 0.00
	$\langle \sigma_\theta^* \rangle$ (kg m^{-3})	27.87 ± 0.00	27.86 ± 0.00	27.86 ± 0.00	27.87 ± 0.00
	$\langle \Psi^* \rangle$ (Sv)	-2.5 ± 1.4	-0.7 ± 1.4	-3.7 ± 1.2	-1.6 ± 1.1
IB	$\langle T^* \rangle$ ($^{\circ}\text{C}$)	2.82 ± 0.01	3.27 ± 0.08	3.11 ± 0.04	2.77 ± 0.03
	$\langle S^* \rangle$	34.97 ± 0.00	34.99 ± 0.01	34.98 ± 0.00	34.98 ± 0.01
	$\langle \sigma_\theta^* \rangle$ (kg m^{-3})	27.88 ± 0.00	27.85 ± 0.00	27.86 ± 0.00	27.89 ± 0.00
	$\langle \Psi^* \rangle$ (Sv)	-4.1 ± 1.0	-0.7 ± 0.5	-1.8 ± 0.8	-3.1 ± 0.4
CGFZ	$\langle \Psi^* \rangle$ (Sv)	-1.7 ± 0.5	$+0.2 \pm 0.7$	-0.1 ± 0.9	-0.8 ± 1.1

using a step-like bottom topography (either fully as in the control GOSI-z*ps configuration or only at depths $>1,200$ m as in the GOSI-szt simulation) seems to introduce large spurious diapycnal mixing, excessively diluting the overflows along their descending paths. The shallow transition from smooth to stepped bathymetry of the GOSI-szt configuration seems to mitigate some overflow biases (e.g., volume transport or hydrography in the IB), while having small negative impact on others (e.g., hydrography in the IS).

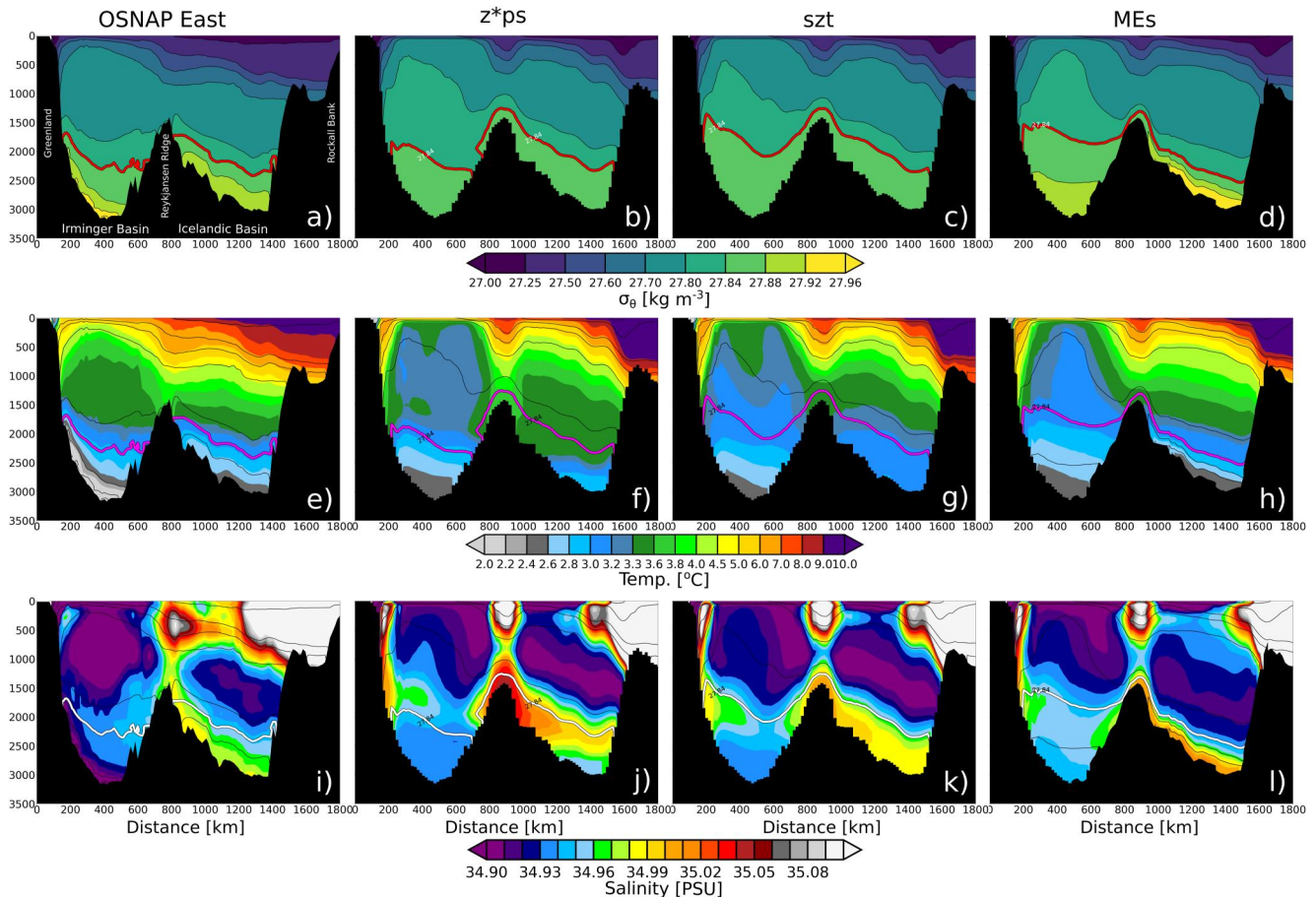


Figure 14. Potential density anomaly (upper row), temperature (middle row) and salinity (bottom row) fields observed (1st column) and simulated by the GOSI-z*ps (2nd), GOSI-szt (3rd column) and GOSI-MEs (4th column) configurations in the Irminger Sea (IS) and Icelandic Basin (IB) cross-sections (see Figure 1 for their locations). The red, magenta and white lines show the 28.84 kg m^{-3} isopycnal.

Our analysis also shows that important biases seem to affect the downstream hydrography of the overflows simulated by the three configurations, with discrepancies from observations that are buoyancy compensated and sometimes larger in the case of the models using localized GVCs (e.g., salinity in the IS section of GOSI-*szt* and GOSI-*MEs*).

5.4. Hydrographic Biases at the Bottom and Overflow Pathways

The aim of this Section is to better understand the origin of the large upstream and downstream biases presented in Sections 5.2 and 5.3. Figure 15 compares the 2014–2018 bottom temperature and salinity fields simulated by the GOSI-*z*ps*, GOSI-*szt*, and GOSI-*MEs* configurations in the Nordic overflows region against the ones from 2005 to 2017 WOA18 climatology (Boyer et al., 2018) while Figure 16 presents the inter-models' differences for the bottom hydrography.

The GOSI-*z*ps* configuration shows important bottom biases in both basins (Figures 15b and 15f). The bottom temperature of the deep part of the IS and along the continental slope of Greenland is generally significantly warmer than WOA18 climatology, with anomalies between ≈ 0.7 and 1.2°C . Similarly, at the bottom of the IB and along the east flank of the RR a warm bias of ≈ 0.5 – 0.7°C exists. The GOSI-*z*ps* bottom waters show also a strong salinity bias at depths around 1,500–2,000 m along the continental slope of both the IS and IB, with errors of ≈ 0.07 – 0.10 and ≈ 0.04 – 0.06 , respectively. Noteworthy, at larger depths the GOSI-*z*ps* bottom salinity is far more similar to the WOA18 climatology in both basins, with average differences ≤ 0.01 .

In the case of the GOSI-*MEs* configuration, the bottom temperature is significantly more accurate than the other two configurations (Figure 15d), with improvements over GOSI-*z*ps* $\geq 0.5^\circ\text{C}$ in the IB and in the range ≈ 0.1 – 0.5°C for the bottom temperature along the continental slope of Greenland at depths around 1,000–2,500 m. In the deepest part of the IS the three configurations seem to be equivalent for the bottom temperature, with differences that are $\leq 0.1^\circ\text{C}$ (see Figures 15 and 16). For salinity, the GOSI-*MEs* configuration presents a bottom positive salinity bias at depths $\geq 2,000$ m in both the IS and IB, with anomalies that are between 0.02 and 0.07, up to ≈ 0.06 larger than the GOSI-*z*ps* error. Contrarily, for depths between $\approx 1,000$ and 2,000 m along the continental slope of both the IS and IB, the GOSI-*MEs* configuration shows better accuracy for the bottom salinity than the control GOSI-*z*ps*, with improvements in the 0.02–0.05 range.

The GOSI-*szt* configuration presents temperature and salinity differences with GOSI-*z*ps* that are generally similar to the ones of GOSI-*MEs* in terms of spatial distribution, but typically much weaker (see Figures 15c, 15g, 16a, 16c, 16d, and 16f). In particular, the bottom temperature of GOSI-*MEs* shows improvements over GOSI-*szt* $\geq 0.5^\circ\text{C}$ in the IB and up to $\approx 0.3^\circ\text{C}$ in the IS for depths between 2000 and 2,500 m (Figure 16c). In the case of salinity, the GOSI-*szt* and GOSI-*MEs* configurations show similar improvements (average differences are < 0.01) over GOSI-*z*ps* along the continental slope of the IS and IB for depths in the range $\approx 1,000$ –2,000 m, while at greater depths the GOSI-*MEs* configuration shows larger salinity biases.

WOA18 climatology describes bottom temperature values of ≈ 4 – 5°C in the proximity of the Denmark Strait sill and ≈ 5 – 6°C in the Iceland-Faroe-Ridge (see Figure 15a) and all our three configurations show large cold bottom biases in these areas (Figures 15b–15d). Interestingly, the analysis presented in Section 5.2 pointed out the opposite, that is, that our three configurations present a consistently warmer bottom temperature than the DS and IFR observed cross-sections, where the measured average overflow water temperature is $\leq 1^\circ\text{C}$ in the DS and $\approx 2.5^\circ\text{C}$ in the IFR (see Table 2). We think this incongruence might be a consequence of the coarse horizontal and vertical resolution of WOA18 data on the shelf. However, in the case of the Denmark Strait sill, the large cold biases of our configurations might be an indication of problems with the NEMO implementation of the Griffies et al. (1998) formulation for the iso-neutral diffusion, as reported by Colombo (2018) for the case of 1/12° regional model of the Greenland-Scotland ridge area. In Appendix D we investigate this possibility.

We continue the analysis presenting in Figure 17 maps of the volume transport and layer thickness of the overflowing dense waters ($\sigma_\theta \geq 27.84 \text{ kg m}^{-3}$) as reproduced by the three configurations.

The ISOW of the GOSI-*MEs* simulation is in good agreement with observations, descending along the east flank of the RR and the deep part of the basin and leaving the IB via gaps in the RR or flowing through the CGFZ (see Figure 1), as shown by the circulation patterns of Figure 17c and the spreading pathways of the differences for the bottom tracers between GOSI-*MEs* and GOSI-*z*ps* configurations of Figures 16b and 16e (the latter are also in very good agreement with the overflow pathways analysis presented in Figure 3 of S. M. Lozier et al. (2022)).

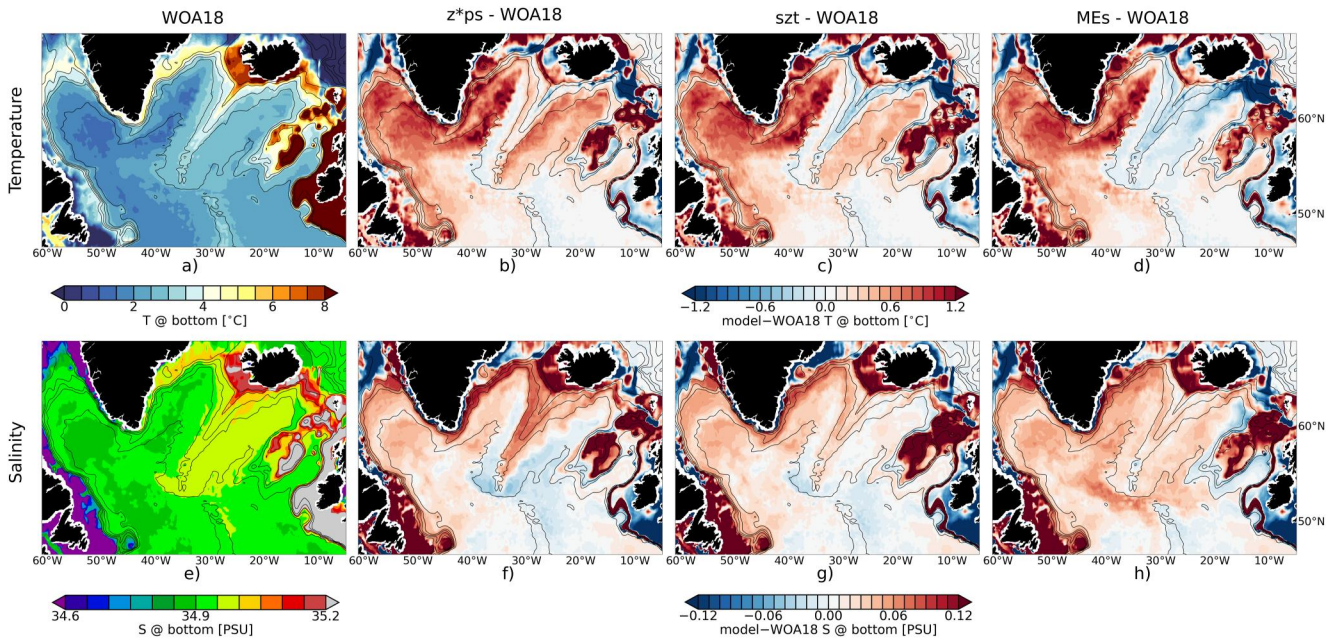


Figure 15. Upper row: bottom temperature field in the Nordic Seas region from 2005 to 2017 WOA18 climatology (a) and differences (model-WOA18) with GOSI-z*ps (b), GOSI-szt (c) and GOSI-MEs (d) configurations. Bottom row: same as in the upper row but for the bottom salinity. Black thin lines identify the 500, 1,000, 1,500, 2,000, and 3,000 m isobaths.

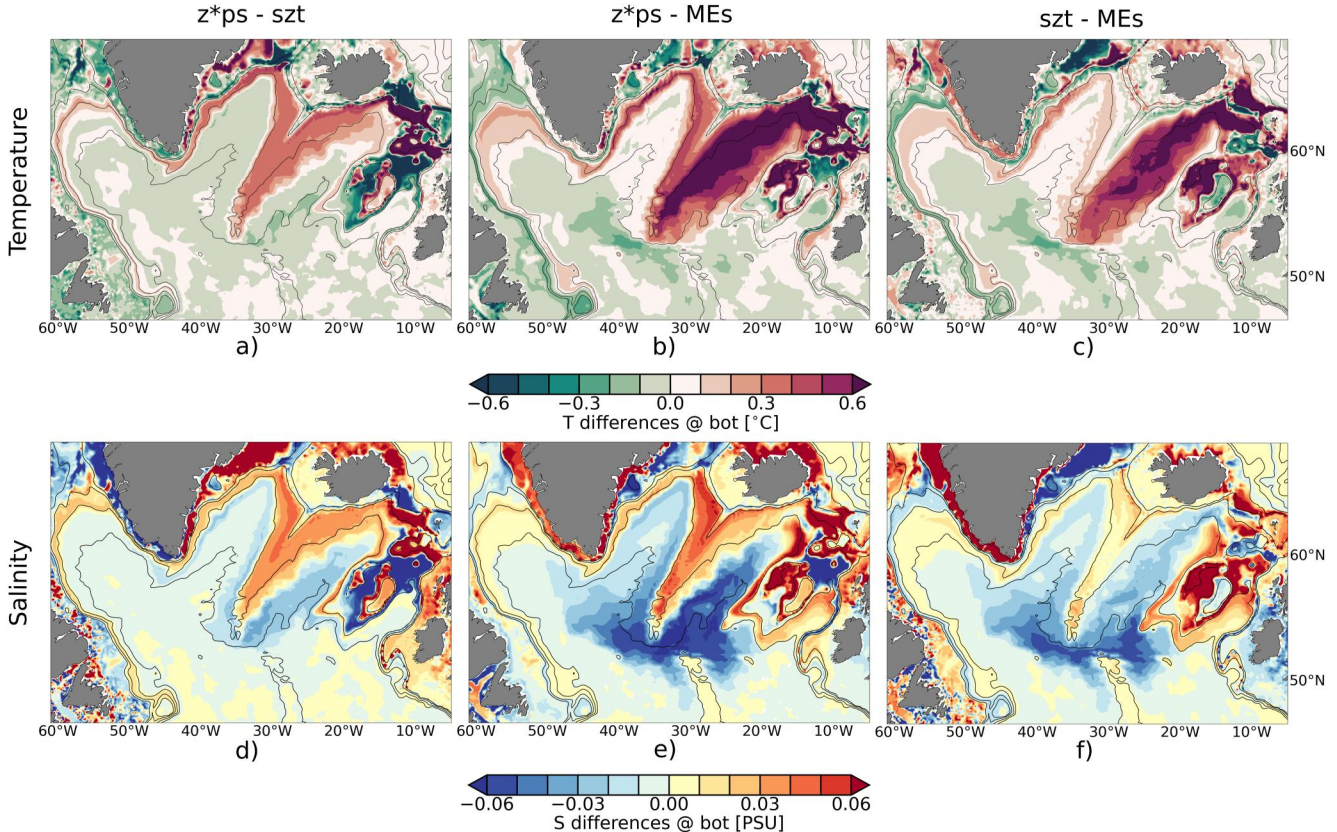


Figure 16. Differences between the control GOSI-z*ps configuration and the GOSI-szt and GOSI-MEs configurations for the bottom temperature (upper row) and salinity (bottom row). Black thin lines identify the 500, 1,000, 2,000, and 3,000 m isobaths.

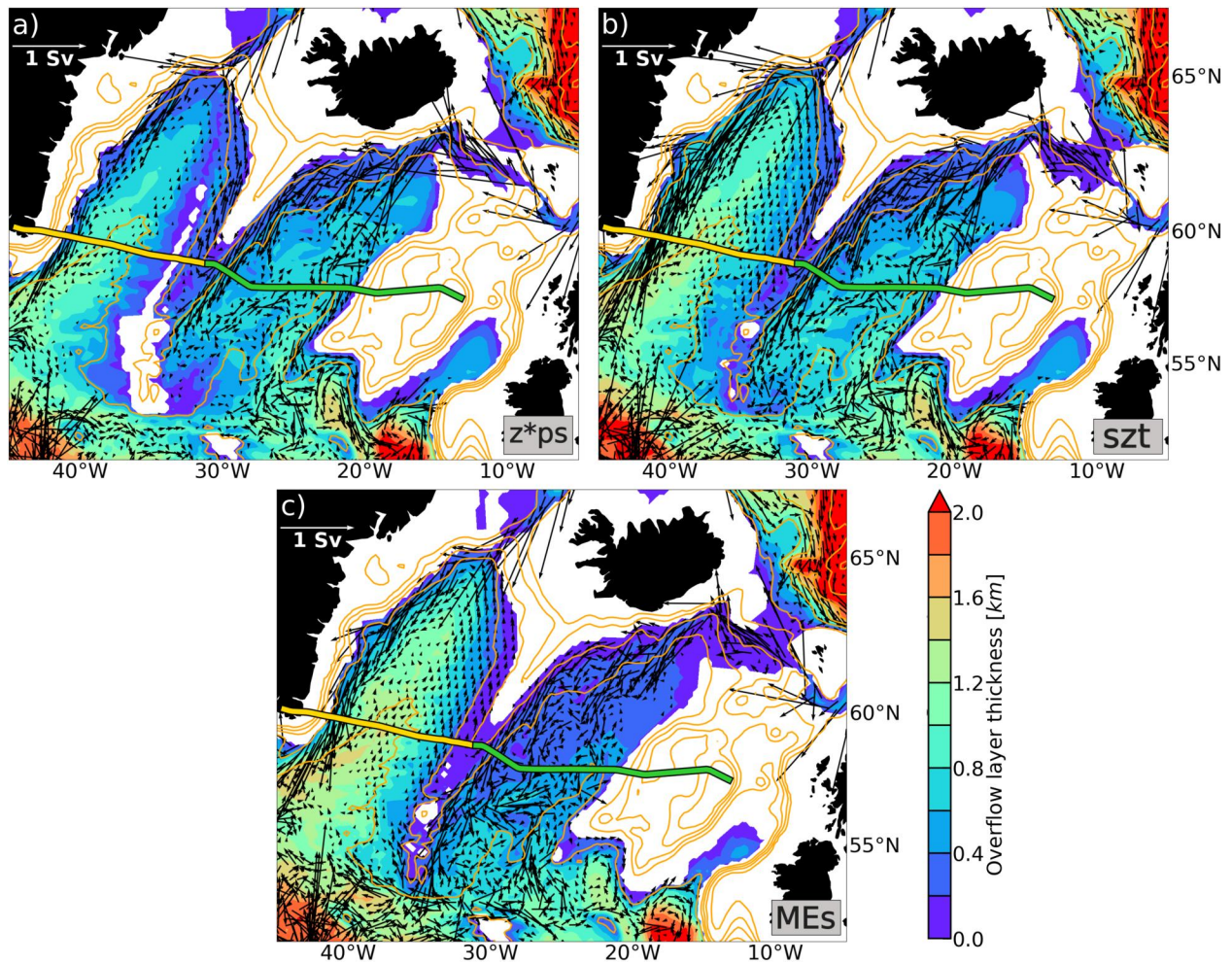


Figure 17. Layer thickness and associated volume transport of overflowing dense waters ($\sigma_\theta \geq 27.84 \text{ kg m}^{-3}$) for the GOSI- z^*ps (a), GOSI- szt (b) and GOSI-MEs (c) configurations. Thick yellow and green lines show the location of the IS and IB sections, respectively. Thin yellow lines present the 500, 1,000, 1,500, 2,000, and 3,000 m isobaths.

To the contrary, in the GOSI- z^*ps and GOSI- szt configurations the IB overflow flows along a narrower part of the east side of the RR, presents a weaker transport (especially in the control configuration) and leaves the IB only via the RR, with no circulation through the CGFZ (see Figures 16a, 17a, and 17b and Table 3).

In the IS, the GOSI- z^*ps configuration simulates a narrow and thin overflow water mass flowing along the continental slope of Greenland with weak transport and confined below the 2,000 m isobath, while in the GOSI- szt experiment the DSOW flow is much stronger and intersects the $\approx 1,000\text{--}2,000$ m depth range. GOSI-MEs reproduces a DSOW flowing at depths $\geq 2,000$ m as the GOSI- z^*ps configuration but with a much stronger transport, similar to the one of the GOSI- szt simulation.

In general, the net southward transport reproduced by the GOSI- szt and GOSI- z^*ps configurations in the IS is significantly larger than the one of the GOSI-MEs simulation (see Figure 12a). As already demonstrated in the idealized experiments (see Figure 10), this can be attributed to the fact that in GOSI-MEs the Ekman bottom transport is better represented, breaking geostrophy and hence increasing the down-slope component of the flow. The net southward transport of GOSI- z^*ps between 27.80 and 27.85 presented in Figure 12a is much larger than the ones of the other two models: this is probably a consequence of the fact that in the GOSI- z^*ps configuration the deep northward flow entering the IS is very weak, as shown by Figure 17a.

5.5. The Impact of Vertical Coordinates and Model Biases on Overflows Simulations

The tracers biases at the bottom and overflow pathways described in Section 5.4, together with the analysis of the upstream and downstream hydrography and transport presented in Sections 5.2 and 5.3 indicates the following mechanisms for the impact of model biases and type of vertical coordinates on the overflows properties.

The three configurations simulate an ISOW crossing the Greenland-Scotland ridge with broadly similar hydrographic and transport characteristics, in reasonable agreement with the observations (see Section 5.2). When descending along the continental slope of the IB, the ISOW of the three configurations mixes with local waters that are generally moderately warmer and saltier than the observations.

Because of the step-like bottom topography and the way gravity currents are represented in geopotential coordinates, the ISOW of the GOSI- z^* ps configuration experiences large mixing while flowing down the IB. As a result, the GOSI- z^* ps simulation reproduces an IB overflow that is not dense enough ($\sigma_\theta < 27.84 \text{ kg m}^{-3}$) to penetrate at depth and remains confined in a narrow part of the east side of the RR (Figures 14b, 14f, 14j, 15b, and 15f and Table 3).

In contrast, the smooth representation of the ocean floor typical of GOSI-MEs significantly reduces the undesired numerical mixing during the dense plume descent. As a consequence, when the ISOW of the GOSI-MEs configuration entrains the relatively warm and salty waters of the IB, the result is an overflow that is in good agreement with the observations for temperature but is slightly saltier and hence denser than the measurements (Figures 14d, 14h, 14l, 15d, and 15h and Table 3).

The GOSI- sz t simulation represents an intermediate solution, where numerical mixing is partially reduced in comparison to the GOSI- z^* ps configuration but is still too large to retain a dense modified ISOW similar to the observations (Figures 14c, 14g, 14k, 15c, and 15g and Table 3). Interestingly, GOSI- sz t seems to be able to mitigate the salinity bias affecting the ISOW of the GOSI-MEs simulation. This is probably a compensation error rather than a model improvement due to the higher numerical mixing affecting the GOSI- sz t simulation below the 1,200 m, as indicated by Figures 14k, 14l, 15g, 15h, and 16f.

The DSOW simulated by the three configurations in the proximity of the Greenland-Scotland ridge presents significant positive temperature and salinity biases, that are compensated in terms of buoyancy, resulting in an overflow density very similar to the observations (Figures 13a.*–13d.* and Table 2). In addition, all the three configurations simulate an Irminger current with large salinity biases (i.e., on average >0.15 , see Figure 14) that interacts with the descending DSOW, contributing to increase the salinification of this water mass.

In the GOSI- z^* ps simulation, the excessive numerical diapycnal mixing seems to seriously affect the properties of the dense descending plume. As a result, a relatively light modified DSOW that does not reach the bottom of the IS is created—see the salty plume with $\sigma_\theta < 27.84 \text{ kg m}^{-3}$ that spreads at its neutrally buoyant level in Figure 14j isolating the relatively fresh water mass at the bottom. Consequently, the mid depth flowing modified DSOW mixes with the relatively warm and salty modified ISOW circulating in the IS in the same depth range (see Figure 17a). This can be observed in the peak in transport shown in Figure 12a for densities between 27.80 and 27.85 kg m^{-3} and the large positive active tracers biases of Figure 15 between 1,500 and 2,000 m along the continental slope of Greenland.

In the GOSI-MEs experiment, the cascading DSOW experiences significantly reduced numerical mixing and entrains the relatively cold and salty modified ISOW flowing in the IS at depths between 1,500 and 2,500 m—see, for example, the propagation paths of the cold and salty anomalies with respect to GOSI- z^* ps and GOSI- sz t configurations presented in Figures 16b, 16c, 16e, and 16f, respectively. As a result, a modified DSOW with an average σ_θ in good agreement with the observations that reaches the bottom of the IS is created, as shown in Figure 14d and Table 3. Because of the hydrographic biases already affecting the DSOW upstream and the Irminger current, improvements in temperature at the bottom of the IS in comparison to the other two configurations are small (Figures 16b and 16c), while salinity errors are slightly more pronounced (Figures 16e and 16f).

Also in the IS the GOSI- sz t solution represents a hybrid between the GOSI- z^* ps and GOSI-MEs simulations—see for example, the temperature and salinity anomalies with respect to GOSI- z^* ps (Figures 16a and 16d)

and GOSI-MEs (Figures 16c and 16f) simulations. Since numerical mixing is reduced only at depths shallower than 1,200 m, GOSI-*szt* simulates a modified DSOW with $\sigma_\theta > 27.84 \text{ kg m}^{-3}$, but one that is not dense enough to reach the bottom of the IS, therefore spreading laterally at its neutral buoyancy level and isolating the relatively cold and fresh water of the initial condition as in the GOSI-*z**ps case (see Figures 14c, 14g, and 14k).

Finally, our results show that the impact of changing the vertical coordinate system seems to extend beyond the boundaries of the localization area, affecting also the hydrographic properties of the DWBC in the Labrador Sea and along the eastern continental slope of North America as indicated by Figure 16.

In summary, the following main points result from our analysis:

- The three configurations present similar temperature and salinity biases that compensate in buoyancy;
- Biases affecting the modified ISOW seem to play an important role in pre-conditioning the overflow biases in the IS;
- The GOSI-MEs configuration is able to reduce the large mixing affecting the configurations using *z**ps-levels, retaining the dense overflow signal at depth as expected. However, as a result, tracers biases at the bottom are exacerbated in the GOSI-MEs simulation, especially for the case of salinity;
- In the GOSI-*z**ps and GOSI-*szt* experiments the large numerical mixing combines with models biases to generate modified ISOW and DSOW water masses that are too warm and not dense enough but at the same time not as saline as the ones of the GOSI-MEs simulation, especially at the bottom;
- The impact of using local-GVC in the Nordic Seas overflow region extends to the entire subpolar gyre.

6. Conclusions and Perspectives

A simple methodology to smoothly blend between different types of quasi-Eulerian generalized vertical coordinates in the horizontal direction is introduced. We refer to it as *localization* method, since it allows one to change the type of vertical coordinate system in arbitrarily chosen time-invariant localized areas of numerical ocean models. The result is a quasi-Eulerian coordinate system that is hybrid in the horizontal direction, similar to how some coordinates are hybrid in the vertical. One of the main aims of the *localization* method proposed in this study is to improve the ocean models' representation of the important influence the bottom topography exerts on the oceanic flow.

After detailing the characteristics of the novel method, in this study we test its ability to improve the Nordic Seas overflows representation in a NEMO-based eddy-permitting global ocean configuration. Three state-of-the-art *z**-coordinate, with partial steps (*z**ps), configurations localizing different types of hybrid geopotential/terrain-following vertical coordinates in the proximity of the Greenland-Scotland ridge are compared against a control employing *z**ps levels everywhere. The quasi-Eulerian vertical coordinates tested in the Greenland-Scotland ridge localization area are the hybrid vanishing quasi-sigma (vqs), *szt*-transitioning (*szt*) or multi-envelope *s* (MEs) coordinates.

Two idealized numerical experiments and a realistic 10-year long simulation are conducted. The idealized experiments aim at assessing the ability of the models to accurately compute horizontal pressure forces (HPG tests) and reduce spurious diapycnal mixing when simulating dense water cascading down the steep continental slope of the Irminger Sea (OVF tests). The realistic runs seek to evaluate the models' skill in reproducing observed hydrographic and transport properties of the Nordic overflows.

Numerical experiments indicate that the localization approach proposed in this study can be successfully used to embed terrain-following levels in a global ocean configuration otherwise using quasi-Eulerian geopotential-based vertical coordinates, provided that the localized coordinate system chosen is flexible enough to allow a smooth transition between the two (as in the MEs and *szt* cases, for example).

In particular, the HPG tests show that the vqs approach might be not convenient for the configuration proposed in this study (i.e., vqs embedded in *z**ps), since it generates large ($>0.10 \text{ m s}^{-1}$) spurious currents and undesired bathymetric noise in the areas where it blends with the global coordinate system. Our analysis suggests that the magnitude of such HPG errors might depend on the width of the transition area

and future sensitivity tests might be beneficial to learn the range of applicability of local-vqs coordinates. The same conclusions may apply also to classical σ (e.g., Phillips, 1957) and s (e.g., Song & Haidvogel, 1994) terrain-following coordinates, since they offer a degree of adaptability very similar to the one of hybrid vqs-coordinates. In the case of MEs and sz vertical coordinates, combining the localization method with the iterative smoothing algorithm described in Appendix C seems to be a viable solution for taking advantage of terrain-following levels in global ocean configurations while limiting errors in the computation of horizontal pressure forces. However, the results of the idealized HPG experiments pointed out that, in order for the iterative smoothing algorithm to be truly effective, the HPG tests must be long enough to allow the spurious currents to fully develop everywhere in the domain.

The idealized OVF tests and the realistic experiments show that localizing terrain-following MEs coordinates in the Greenland-Scotland ridge region allows important reduction of cross-isopycnal mixing when modeling bottom intensified buoyancy driven currents, significantly improving the realism of Nordic overflows simulations in comparison to the configurations using z^* ps or sz coordinates, especially in term of density and transport. The impact of changing vertical grid propagates well beyond the boundaries of the Greenland-Scotland ridge localization area, extending to the entire subpolar gyre, demonstrating the robustness and efficacy of the localization method.

Important hydrographic biases similarly affect all the realistic experiments. In the case of the configurations using geopotential-based levels at depth, the large numerical mixing results in a secondary compensating effect that mitigates the models' biases at the bottom, especially for salinity. To the contrary, the ability of the configuration using local-MEs levels to importantly reduce spurious mixing exacerbates the salinity biases at the bottom. These results indicate that the Nordic region of our eddy-permitting global configuration is affected by biases that can not be mitigated using a vertical grid targeting the local leading processes, especially in the case of salinity. Other studies have reported important salinity biases affecting NEMO-based simulations of the North Atlantic subpolar gyre (e.g., Marzocchi et al., 2015; Rattan et al., 2010; Treguier et al., 2005). A special North Atlantic processes evaluation group (NatlPEG) involving the UK Met Office and National Oceanography Centre is currently investigating possible large scale causes behind those biases.

The localization method proposed in this paper is general, in the sense that can be easily applied to any region of any quasi-Eulerian model domain. For example, applications to improve the representation of boundary currents and the shelf dynamics in global ocean configurations are currently being tested. Similarly, the localization method is also being implemented with promising results in a regional set-up to embed MEs coordinates in a model using vqs levels for improving the shelf dynamics.

Finally, possible future developments include using the localization method to make it easier changing type of vertical grid in AGRIF (Debreu et al., 2008, 2012) nests or combining a local-MEs coordinate system with the Brinkman penalization approach (Debreu et al., 2020), considering that both methods rely on the definition of envelope(s) of the bottom topography.

Appendix A: A Simple Algorithm for Defining Transition Areas

Let us consider a model domain with horizontal coordinates x and y . A generic localization area Λ can be defined by an indicator function $\mathbb{1}_{\Lambda}(x,y)$,

$$\mathbb{1}_{\Lambda}(x,y) = \begin{cases} 1 & \text{if } (x,y) \in \Lambda, \\ 0 & \text{otherwise.} \end{cases} \quad (\text{A1})$$

Then, the generic transition area T encircling the localization area Λ is computed in this study according to the following algorithm:

```

/* Define B such that B(x,y) is 1 if (x,y) ∈ Λ and 1 + γ if not; */
B = J + γ(J - 1Λ);
/* Initialise the 'working' variable W; */
W = B;
/* Initialise the iterator variable n; */
n = 0;
/* Main loop; */
while n ≤ niter do
  /* Apply a Gaussian low-pass filter G to W to smoothly blend
  between the localisation area Λ and the rest of the domain and
  obtain the filtered function W̄; */
  W̄ = G ★ W;
  /* W(x,y) is updated to be equal to W̄(x,y) only outside the
  localisation area Λ; */
  W = 1Λ + (J - 1Λ) ○ W̄;
  /* Advance the iterator variable; */
  n+ = 1;
end
/* D results to be > 0 only in the transition area T; */
D = |W - B|;

```

where B is a modified version of 1_{Λ} where zeros are substituted with $1 + \gamma$, $J = 1$ is a constant function, γ represents any number > 0 (sensitivity tests showed that the algorithm is not very responsive to different values of this parameter), W is a “working” variable, n_{iter} is the user-defined maximum number of iterations and $G(x_0, y_0, \sigma_G, x, y)$ is a two-dimensional spatial Gaussian filter with σ_G the user-defined width of the filter and \circ describing the Hadamard product (i.e., the element-wise matrix product, Horn and Johnson (1985)).

The value of the filtered function $\bar{W}(x, y)$ after the Gaussian low-pass filtering operation $G \star W$ at a point (x_0, y_0) is given by

$$\bar{W}(x_0, y_0) = G \star W = \iint W(x, y) G(x_0, y_0, \sigma_G, x, y) dx dy \quad (A2)$$

$$= \frac{1}{2\pi\sigma_G^2} \iint W(x, y) \exp\left\{-\frac{(x-x_0)^2 + (y-y_0)^2}{2\sigma_G^2}\right\} dx dy \quad (A3)$$

The transition area T is then defined by the indicator function $1_T(x, y)$,

$$1_T(x, y) = \begin{cases} 1 & \text{if } D(x, y) > 0 \\ 0 & \text{otherwise.} \end{cases} \quad (A4)$$

While both σ_G and n_{iter} parameters control the width of the transition area T (for both variables a larger value leads to a wider transition zone), n_{iter} has a higher impact than σ_G . In this work, the transition area is generated using $\gamma = 1.0 \times 10^{-10}$, $\sigma_G = 1$, and $n_{iter} = 1$.

Appendix B: Quasi-Eulerian Coordinates Transformations

This section describes the QE GVCs implemented in this study. We focus on the details of the analytical coordinate transformations since in the case of vqs, sgt and MEs coordinates the continuous formulations consistent with an $\alpha_k = h_k^0 H^{-1}$ when discretized are not clear in the current literature. However, we note that the approach to implement QE coordinates and define and evolve in time h_k is dependent on the numerical ocean model code employed. For example, in the case of NEMO, QE GVCs are implemented defining discrete model levels with

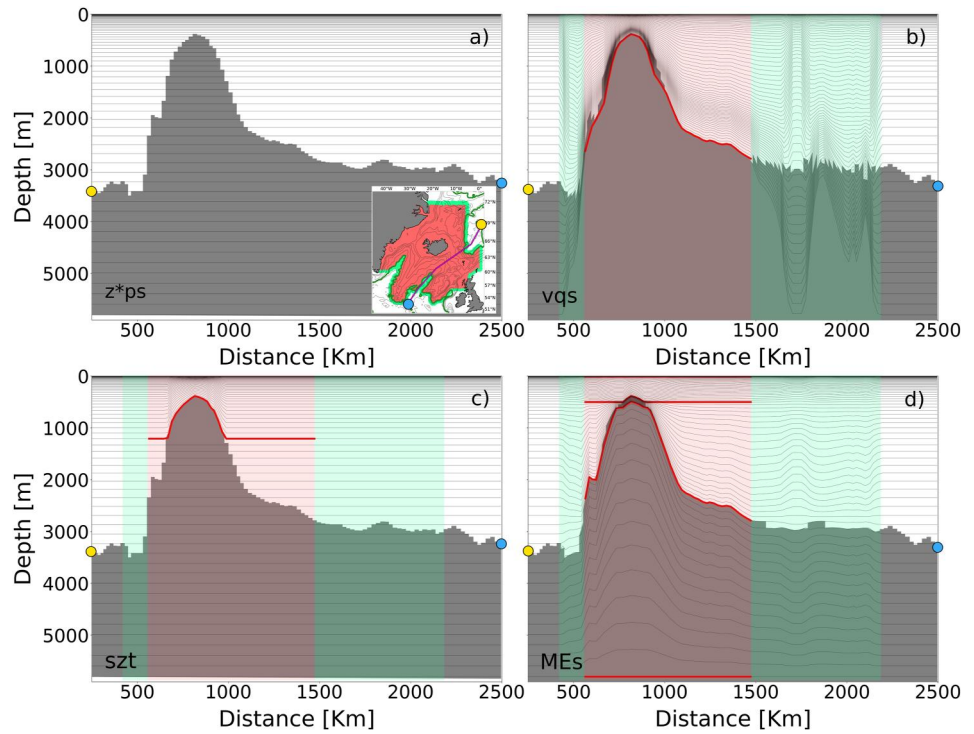


Figure B1. Panel (a) shows the model bathymetry cross-section extracted from the GOSI- z^* ps model, panel (b) from the GOSI- vqs model while panel (c) and (d) from the GOSI- szt and GOSI- MEs models, respectively. In the inset in panel (a), the red and green regions represent the Nordic overflows localization and transition areas used in this study, respectively, the magenta line shows the location of the model bathymetry cross-sections presented in the other panels while the green line marks the 2,800 m isobath. In panels (a–d) the red lines show the location of the envelopes used to configure the localized GVCs while the yellow and cyan points show the beginning and the end of the cross-sections to indicate the direction of increasing distance in the inset in panel (a).

respect to an unperturbed ocean at rest (i.e., $\mathbf{u} = 0, \eta = 0$) and then the variable volume layer algorithm of Levier et al. (2007) is used to evolve h_k according to Equation 4 with $\alpha_k \propto h_k^0 H^{-1}$.

B1. z^* -Coordinate

The NEMO implementation of the z^* -coordinate transformation follows Stacey et al. (1995) and Adcroft and Campin (2004):

$$z = \eta + z^* \frac{H + \eta}{H}, \quad (\text{B1})$$

with $z^*(z = \eta) = 0$ and $z^*(z = -H) = -H$ (see Figures 4b and B1a).

B2. vqs -Coordinate

The standard NEMO v4.0.4 implementation of vqs coordinates is used in this study (see Figures 4c and B1b), which combines modified versions of the QE GVCs originally proposed by Dukhovskoy et al. (2009) and Song and Haidvogel (1994):

$$z = \eta \left[1 + \frac{h_c}{H_e} \sigma + \left(1 - \frac{h_c}{H_e} \right) C(\sigma) \right] + h_c \sigma + C(\sigma)(H_e - h_c), \quad (\text{B2})$$

where $\sigma(z = \eta) = 0$ and $\sigma(z = -H_e) = -1$, $C(\sigma)$ is the Song and Haidvogel (1994) stretching function, H_e is a smooth envelope bathymetry (positive downward and such that $H_e \geq H$) and h_c is the depth at which the transition

from stretched to uniform distributed levels occurs. Equation B2, differently from the original s -coordinates of Song and Haidvogel (1994), ensures that α_k of Equation 4 is a function of h_k^0 and the maximum model depth H_e .

A similar set-up to Colombo (2018) is applied for localizing vqs levels in the Nordic overflows area, using $\theta = 6.0$, $b = 0.7$, and $h_c = 50$, with θ and b the parameters controlling the model levels' distribution near the surface and the bottom, respectively, with the Song and Haidvogel (1994) stretching function.

B3. szt -Coordinate

The szt scheme described in Wise et al. (2021) allows one to combine vqs and z^* ps QE coordinates (see Figures 4d and B1c). The szt analytical formulation reads

$$z = \begin{cases} \eta \left[1 + \frac{\tilde{h}_c}{H_e} \sigma + \left(1 - \frac{\tilde{h}_c}{H_e} \right) Z(\sigma) \right] + \tilde{h}_c \sigma + Z(\sigma) (H_e - \tilde{h}_c) & \text{for } H \leq H_t, \\ \eta + z^* \frac{H + \eta}{H} & \text{for } H > H_t, \end{cases} \quad (\text{B3})$$

where H_t is the depth at which the transition from vqs to z^* coordinates occurs, H_e is a smooth envelope bathymetry with maximum depth H_t and $\sigma(z = \eta) = 0$, $\sigma(z = -H_t) = -1$, $z^*(z = \eta) = 0$, and $z^*(z = -H) = -H$. The standard NEMO formulation for vqs-coordinates (B2) is modified by replacing $C(\sigma)$ with $Z(\sigma)$, a stretching function consistent with the one of Madec et al. (1996), and using the variable \tilde{h}_c defined as

$$\tilde{h}_c = \min \left\{ \max \left\{ \frac{H_e - H_t}{1 - \frac{H_t}{h_c}}, 0 \right\}, h_c \right\}. \quad (\text{B4})$$

When discretizing, the smoothness of h_k is retained by ensuring that discrete vqs and z^* levels are distributed along the water column according to a consistent stretching function.

In practise, the following algorithm is used to generate a szt grid. At first, the k_t z^* -level at which the transition will occur is chosen (in the case of this paper, $k_t = 48$). Then, a standard z^* ps vertical grid is generated. After, an envelope bathymetry H_e with maximum depth $H_t = \max\{z_{k_t}\}$ is computed and used to recompute the depth of all the discrete model levels with $k < k_t$.

B4. MEs-Coordinate

The ME method of Bruciaferri et al. (2018) defines n arbitrary depth surfaces $H_e^i(x, y, t)$ (downward positive) called *envelopes* (with $1 \leq i \leq n$) to divide the ocean model vertical domain into n sub-zones D_i , each one bounded by envelopes H_e^{i-1} at the top and H_e^i at the bottom (with $H_e^0 = -\eta$). Each envelope moves with the free surface according to

$$H_e^i = H_{e_0}^i - \eta \left(1 - \frac{H_{e_0}^i}{H_e} \right), \quad (\text{B5})$$

where $H_{e_0}^i(x, y)$ is the depth with respect to an unperturbed ocean at rest and $H_e = H_{e_0}^n \geq H$.

ME s -coordinates are implemented in the Greenland-Scotland ridge local area using four envelopes and the following coordinate transformation (see Figures 4e and B1d):

$$z|_{D_i} = \begin{cases} C_i(\sigma_i) (H_e^i - H_e^{i-1} - h_c^i) - H_e^{i-1} + h_c^i \sigma_i + \eta \beta_i & \text{if } i \in \{1, 3\}, \\ P_{x,y,i}^3(\sigma_i) \left(1 + \frac{\eta}{H_e} \right) & \text{if } i \in \{2, 4\}, \end{cases} \quad (\text{B6})$$

where $\sigma_i(z = -H_e^{i-1}) = 0$ and $\sigma_i(z = -H_e^i) = -1$, $C_i(\sigma_i)$ is a generic stretching function applied in sub-zone D_i and h_c^i is the depth at which the transition from stretched to uniform distributed levels occurs. The term β_i , defined as

$$\beta_i = \frac{h_c^i}{H_e} \sigma_i - \frac{h_c^i}{H_e} C_i(\sigma_i),$$

ensures that α_k of Equation 4 is a function of h_k^0 and the maximum model depth H_e . The function $P_{x,y,i}^3(\sigma_i)$ represents a complete cubic spline whose coefficients are computed ensuring the monotonicity and continuity of the Jacobian of the transformation for the case of an unperturbed ocean at rest (see Bruciaferri et al. (2018) for the details).

In this study we set $h_c^i = 0$ while the Song and Haidvogel (1994) stretching functions $C_1(\sigma_1)$ and $C_3(\sigma_3)$ use $\theta_1 = 1.2$, $b_1 = 0.7$ and $\theta_3 = 2.4$, $b_3 = 0.85$, respectively (for each sub-zone D_i , θ_i , and b_i control the stretching near the shallower envelope H_e^{i-1} and the deeper envelope H_e^i , respectively). The first envelope $H_{e_0}^1$ has depth equal to 10 m, so that the upper sub-zone D_1 can be discretized with a constant high resolution consistent with the global z^* ps grid. Envelope $H_{e_0}^2$ follows a smoothed version of the bottom topography H from a minimum depth of 40 m to a maximum depth of 500 m: in this way, sub-zone D_2 can use nearly terrain-following levels where $40 \text{ m} \leq H \leq 500 \text{ m}$ to better resolve shelf cascading, while elsewhere can employ z^* -like interfaces to minimize HPG errors. Similarly, the envelope $H_{e_0}^3$ follows the smoothed model bathymetry in areas where $610 \text{ m} \leq H \leq 2,800 \text{ m}$, resulting in terrain-following levels only in areas where the bottom topography is in this depth range to improve overflows simulations. The bottom geopotential envelope $H_{e_0}^4$ targets the depth of last W-level of the global z^* ps grid, so that model levels near the bottom can smoothly transition from the local to the global grid. Envelopes $H_{e_0}^2$ and $H_{e_0}^3$ are smoothed using the iterative algorithm described in Appendix C.

Once the envelopes have been identified based on physical motivations, local MEs-coordinates are discretized assigning to each layers D_i a number of levels which is dictated by the number of levels possessed by the global z^* ps grid at a similar depth range. For example, in this study 9 levels are used in layer D_1 , 31 in D_2 , 20 in D_3 , and 15 in D_4 .

Appendix C: Iterative Algorithm for Smoothing Envelopes Surfaces

The iterative algorithm applied in this study to smooth the envelopes of GOSI-vqs, GOSI-szt and GOSI-MEs configurations use the Martinho and Batteen (2006) smoothing procedure to ensure that the slope parameter $r = |\delta H| (2\bar{H})^{-1}$, with δH the horizontal change in H of adjacent model cells and \bar{H} the mean local bottom depth (Mellor et al., 1998), is smaller than multiple user defined thresholds r_{\max} .

Figure C1 summarizes the main steps of our iterative algorithm. At first, the envelopes of the three GVCs were smoothed by applying the Martinho and Batteen (2006) method with an $r_{\max} = 0.12$. This is a more restrictive value in comparison to the $r_{\max} \approx 0.2$ value typically applied both in basin-scale (e.g., Lemarié et al., 2012) and regional (e.g., Debreu et al., 2022; O’Dea et al., 2012) configurations. After, for each of the GVCs, a series of idealized one month-long HPG tests with a set-up similar to the one described in Section 4.1 were run: at each iteration, the envelopes were smoothed with an increasingly more severe r_{\max} value (i.e., $r_{\max} = 0.075$ and $r_{\max} = 0.04$) only in those grid points where velocity errors exceeded 0.05 m s^{-1} (see text of steps 4, 5, and 6 of Figure C1 for the details). Such a velocity threshold was chosen because it allowed us to significantly smooth the envelopes where HPG errors were large but at same time only marginally affecting areas involved with the overflows descent, as shown in step 5 of Figure C1 for the case of the GOSI-MEs model. Similarly, Wise et al. (2021) used a comparable velocity threshold value, reporting significant benefits in the case of a MEs-coordinates model of the North West European shelf with a lateral resolution of 7 km. In this work, three iterations of the iterative smoothing algorithm were needed to generate the envelopes used to implement the localized GVCs described in Section 3.2.

While in this study we used one month-long HPG tests to identify the grid points where the envelopes needed to be smoothed, the numerical experiments of Section 4.1 showed that such a period was not long enough to have spurious currents fully developed everywhere in the domain. The direct consequence of this was that not all the

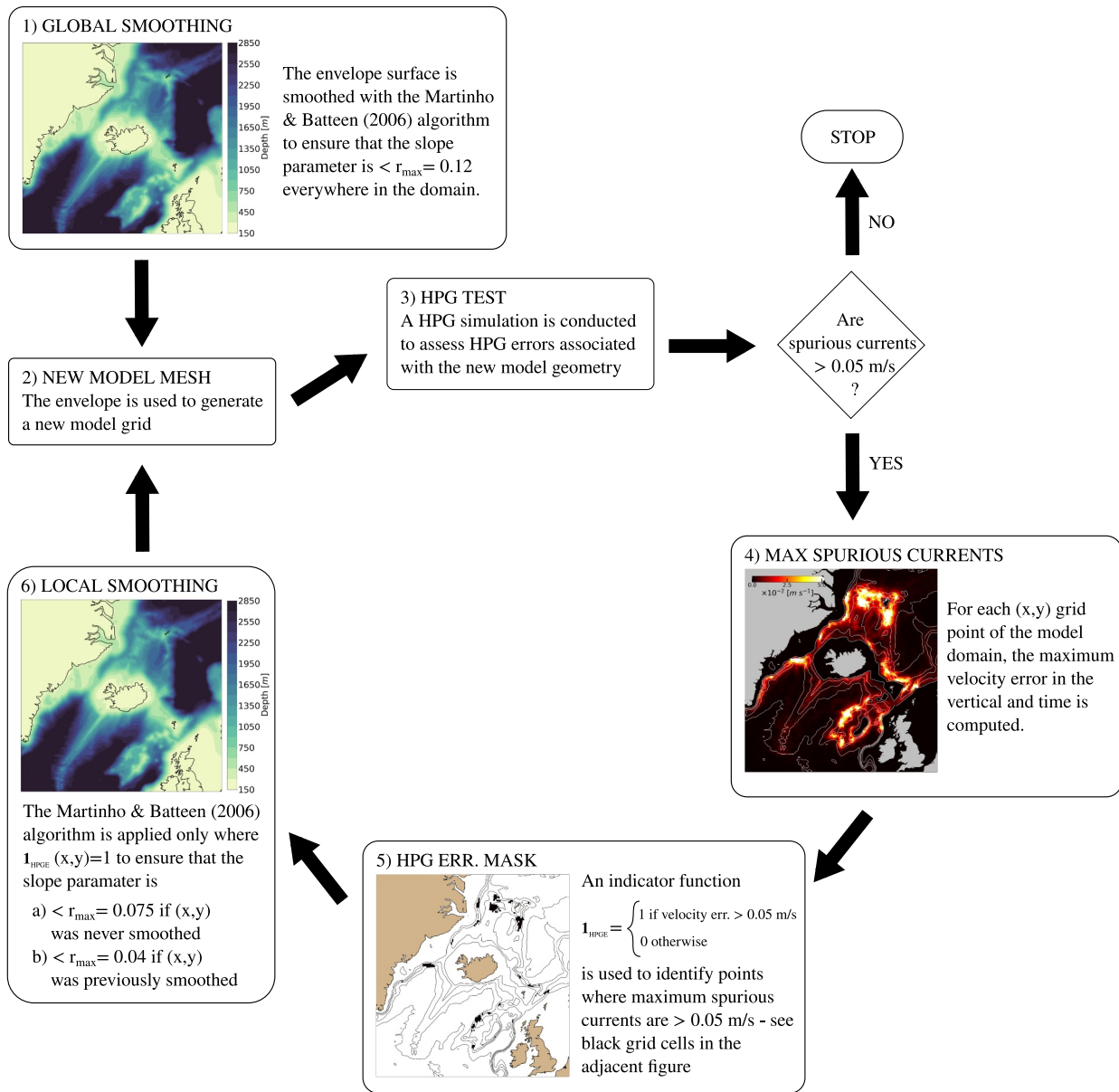


Figure C1. Main steps of the iterative smoothing algorithm applied in this study to smooth the envelopes of vqs, szt and MEs models.

problematic grid points were identified by the algorithm. Therefore, future applications of the iterative smoothing algorithm should first assess the minimum length needed by a HPG test to have fully developed spurious currents where viscosity and friction balance the prognostic growth of the erroneous flow field (e.g., Berntsen, 2002; Berntsen et al., 2015; Mellor et al., 1998).

Appendix D: The Impact of the Iso-Neutral Mixing Formulation in an Eddy-Permitting Configuration

A formulation for the iso-neutral diffusion inspired by Griffies et al. (1998) (hereafter TRIADS) is used in this study, since it is the only available option in NEMO v4.0.4 to correctly compute the slopes between iso-neutral and computational surfaces when using GVCs (Madec & NEMO-team, 2019—p. 120). However, when using the TRIADS formulation in a $1/12^\circ$ NEMO-based regional configuration of the Greenland-Scotland ridge area employing vqs hybrid coordinates, Colombo (2018) reports undershooting issues of the iso-neutral operator

leading to unrealistic low temperature values in the proximity of the Denmark Strait sill ($\approx -1^\circ\text{C}$ when inspecting annual averages).

The upper row of Figure D1 shows that this seems to be the case also in our realistic experiments, where local minima of about $\approx -1^\circ\text{C}$ and $\approx -0.25^\circ\text{C}$ are present near the Denmark Strait sill in the 2014–2018 mean bottom temperature fields simulated by the GOSI- z^*ps and GOSI-MEs models, respectively. The GOSI- szt configuration does not show such unrealistic bottom temperature values, although this might be due to the averaging processing.

The fact that the same issue appears with both standard z^*ps and localized MEs coordinates is enough to prove that this problem is unrelated to our localization method or the use of GVCs.

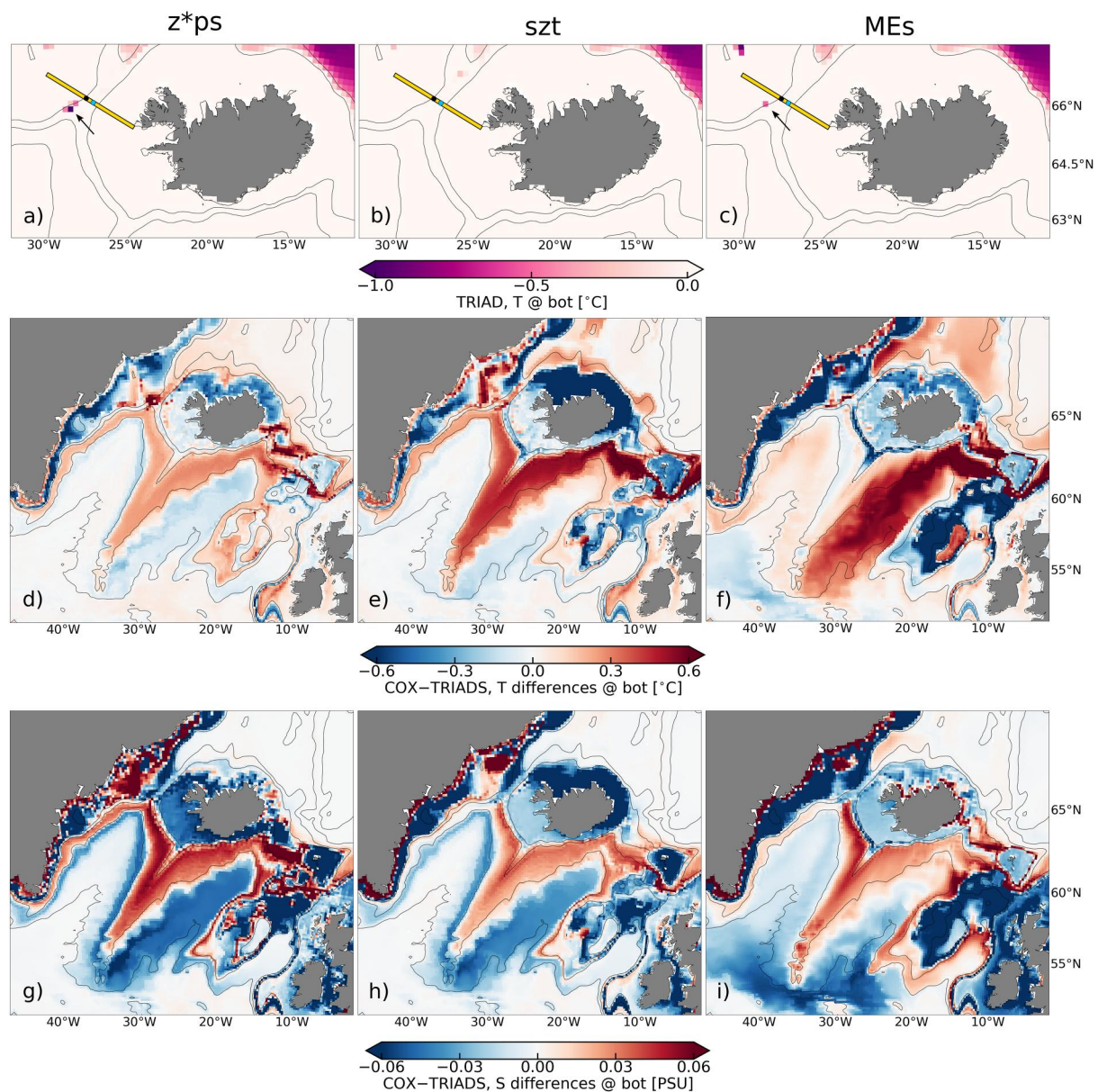


Figure D1. *Upper row:* 2014–2018 mean bottom temperature for values colder than 0°C simulated by the GOSI- z^*ps (a), GOSI- szt (b) and the GOSI-MEs (c) configurations when using the TRIADS formulation for the iso-neutral diffusion; the yellow line represents the DS observational cross-section (see Table 1) while the two black and cyan points represent the location of the two observational temperature profiles shown in Figure D2; *Middle row:* 2014–2018 averaged bottom temperature differences between experiments using either the TRIADS or the COX formulations for the GOSI- z^*ps (d), GOSI- szt (e) and the GOSI-MEs (f) configurations; *Bottom row:* the same as the middle row but for salinity.

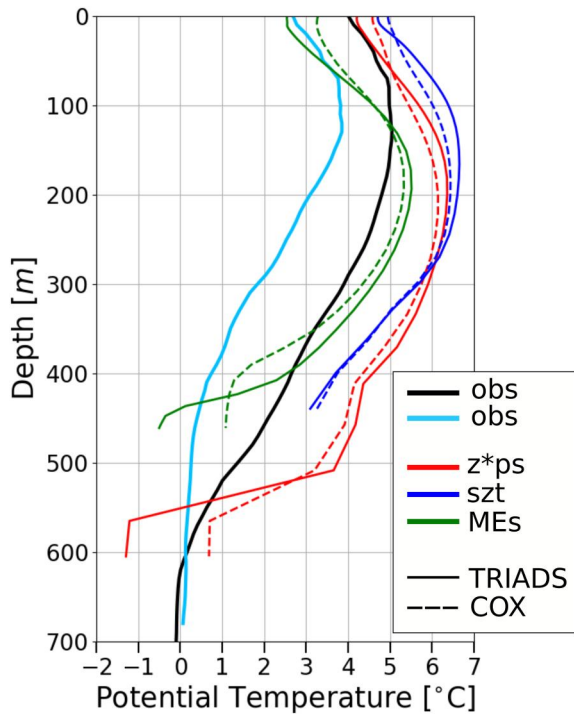


Figure D2. Temperature profiles simulated by the GOSI- z^*ps (red), GOSI- sz_t (blue) and GOSI-MEs (green) configurations and extracted in those locations where maximum undershooting appears in the experiments using the TRIADS formulation (see the arrows in panel (a) and (b) in Figure D1). In the case of the GOSI- sz_t configuration, the same grid point of GOSI-MEs is chosen. The profiles represented with continuous lines are simulated using the TRIADS formulation while the ones shown with dashed lines are from the experiments using the COX formulation. In black and cyan also presented two observational profiles extracted from the DS cross-section (see Table 1) in the black and cyan points shown in the upper row of Figure D1.

However, in order to confirm that this is a problem of the NEMO TRIADS formulation, we decided to conduct three additional numerical experiments running our three GOSI- z^*ps , GOSI- sz_t , and GOSI-MEs configurations with an alternative formulation for the iso-neutral diffusion. NEMO offers only two options for the iso-neutral mixing, the TRIADS scheme and a modified version of the formulation proposed by Cox (1987) (hereafter COX, see Madec and NEMO-team (2019) for the details). As expected, the new additional realistic experiments using the COX formulation did not show any undershooting issues in the proximity of the Denmark Strait sill—for example, Figure D2 compares the temperature profiles extracted in those locations where undershooting appears in the experiments using the TRIADS formulation against the profiles simulated by the three configurations in the same grid points but with the COX formulations.

While switching from the TRIADS to the COX formulation seems to be the solution to avoid those undershooting issues in NEMO, at the same time this simple strategy introduces additional complications when using GVCs. In fact, when using the COX formulation with model levels non aligned with geopotentials and a realistic equation of state, the evaluation of along-levels derivatives includes a pressure dependent part, leading to a wrong evaluation of the neutral slopes (Madec & NEMO-team, 2019—p. 120). The middle and bottom rows of Figure D1 demonstrate the impact of using the COX formulation on the bottom temperature and salinity of our simulations. For the purpose of this paper, it is interesting to observe that in the case of the two GOSI- sz_t and GOSI-MEs models the COX formulation introduces quite strong diapycnal mixing that seems to substantially mitigate the benefits of using terrain-following levels, especially for temperature (Figures D1e and D1f should be compared to Figures 16a and 16b). However, such an important impact of the type of iso-neutral formulation in GVCs is most likely linked to the eddy-permitting nature of our configurations and one would expect that it would reduce at higher resolutions, as reported by Colombo (2018) for the case of a regional model of the Nordic Seas area at $1/60^\circ$ of horizontal resolution.

Interestingly, switching from the TRIAD to the COX formulation seems to have a non-trivial impact also in the case of GOSI- z^*ps .

Appendix E: List of Acronyms

Table E1 is a list of acronyms to assist cross-referencing abbreviations used in the paper.

Table E1 List of Acronyms Used in the Paper	
Acronym	Meaning
<i>Vertical Coordinates</i>	
GVC	Generalized vertical coordinate
QE	quasi-Eulerian
LG	Lagrangian
ALE	Arbitrary Lagrangian Eulerian
z^*ps	z^* -coordinates with partial steps
vqs	Vanishing quasi-sigma
sz_t	Hybrid sz -transitioning
MEs	Multi-Envelope s -coordinates

Table E1

Continued

Acronym	Meaning
<i>Water masses and currents</i>	
AMOC	Atlantic Meridional Overturning Circulation
DSOW	Denmark Strait Overflow Water
ISOW	Iceland-Scotland Overflow Water
NAW	North Atlantic Water
DWBC	Deep Western Boundary Current
<i>Numerical models</i>	
GOSI-025	GOSI global ocean configuration at 1/4° of horizontal resolution
GOSI-z*ps	standard GOSI-025 configuration using z*ps everywhere
GOSI-vqs	GOSI-025 configuration using vqs levels in the Greenland-Scotland ridge area
GOSI-szt	GOSI-025 configuration using szt levels in the Greenland-Scotland ridge area
GOSI-MEs	GOSI-025 configuration using MEs levels in the Greenland-Scotland ridge area
<i>Observational data sets</i>	
OSNAP	Overturning in the Subpolar North Atlantic Program
WOA18	World Ocean Atlas 2018
DS	Denmark Strait cross-section
IS	Irminger sea portion of the eastern leg of the OSNAP cross-section
IB	Icelandic basin portion of the eastern leg of the OSNAP cross-section
IFR	Iceland-Faroe ridge cross-section
FSC	Faroe-Shetland channel cross-section
FBC	Faroe-Bank channel cross-section
WTR	Wyville-Thomson ridge cross-section
CFGZ	Charlie-Gibbs Fracture Zone cross-section
<i>Miscellaneous</i>	
NEMO	Nucleus for European Modeling of the Ocean
HPG	Horizontal pressure gradient

Data Availability Statement

The four models compared in this study are based on the NEMO ocean model code, which is freely available from the NEMO website (<https://www.nemo-ocean.eu>, last access: 22 January 2024). The code to localize quasi-Eulerian general vertical coordinates used in this study is included in the NEMO v4.2 main branch. Additional modifications to the NEMO original code are required for running GOSI-based configurations. The actual NEMO v4.0.4 source code and the namelists used to run the integrations presented in this manuscript are available at Bruciaferri (2023b). The data describing the geometry of the four models and the data used for the analyses and plots included in this manuscript are available at Bruciaferri (2023c) and Harle (2023) while the actual code to reproduce the analysis and the plots can be found at Bruciaferri (2023a) and Almansi and Bruciaferri (2023).

References

- Adero, A., Anderson, W., Balaji, V., Blanton, C., Bushuk, M., Dufour, C. O., et al. (2019). The GFDL global ocean and sea ice model OM4.0: Model description and simulation features. *Journal of Advances in Modeling Earth Systems*, 11(10), 3167–3211. <https://doi.org/10.1029/2019MS001726>
- Adero, A., & Campin, J.-M. (2004). Rescaled height coordinates for accurate representation of free-surface flows in ocean circulation models. *Ocean Modelling*, 7(3–4), 269–284. <https://doi.org/10.1016/j.ocemod.2003.09.003>
- Adero, A., & Hallberg, R. (2006). On methods for solving the oceanic equations of motion in generalized vertical coordinates. *Ocean Modelling*, 11(1–2), 224–233. <https://doi.org/10.1016/j.ocemod.2004.12.007>

Acknowledgments

Funding support for DB, CG, and HH was provided by the Joint DECC/Defra Met Office Hadley Centre Climate Programme (GA01101), UK Ministry of Defense and the UK Public Weather Service. JH and MA were supported by the H2020 European Institute of Innovation and Technology (IMMERSE) Grant 821926. The authors would like to thank Mike Bell, Dave Storkey, Nigel Wood, and Jérôme Chanut for helpful and constructive discussions, suggestions, and advice. Numerical simulations and analysis were carried out on the Cray HPC at the Met Office, UK. In addition, the authors would like to thank the three anonymous reviewers for their thorough review of this manuscript and the constructive comments and suggestions that were made—they have greatly contributed to improving this study.

- Almansi, M., & Bruciaferri, D. (2023). JMMP-Group/Nordic-seas-validation: November 17, 2023 release (version 1.0.0) [Software]. Zenodo. <https://zenodo.org/records/10149505>
- Berntsen, J. (2002). Internal pressure errors in sigma-coordinate ocean models. *Journal of Atmospheric and Oceanic Technology*, 19(9), 1403–1414. [https://doi.org/10.1175/1520-0426\(2002\)019\(1403:IPEISC\)2.0.CO;2](https://doi.org/10.1175/1520-0426(2002)019(1403:IPEISC)2.0.CO;2)
- Berntsen, J., Thiem, Ø., & Avlesen, H. (2015). Internal pressure gradient errors in σ -coordinate ocean models in high resolution fjord studies. *Ocean Modelling*, 92, 42–55. <https://doi.org/10.1016/j.ocemod.2015.05.009>
- Bleck, R. (1978). On the use of hybrid vertical coordinates in numerical weather prediction models. *Monthly Weather Review*, 106(9), 1233–1244. [https://doi.org/10.1175/1520-0493\(1978\)106\(1233:OTUOHV\)2.0.CO;2](https://doi.org/10.1175/1520-0493(1978)106(1233:OTUOHV)2.0.CO;2)
- Bleck, R. (2002). An oceanic general circulation model framed in hybrid isopycnic-Cartesian coordinates. *Ocean Modelling*, 4(1), 55–88. [https://doi.org/10.1016/S1463-5003\(01\)00012-9](https://doi.org/10.1016/S1463-5003(01)00012-9)
- Boyer, T. P., Garcia, H. E., Locarnini, R. A., Zweng, M. M., Mishonov, A. V., Reagan, J. R., et al. (2018). *World ocean Atlas 2018* (Technical Report). NOAA National Centers for Environmental Information. Dataset. Retrieved from <https://www.ncei.noaa.gov/archive/accession/NCEI-WOA18>
- Bruciaferri, D. (2023a). JMMP-Group/loc_gvc-GO_ovf: November 17, 2023 (version 1.0.0) [Software]. Zenodo. <https://zenodo.org/records/10149529>
- Bruciaferri, D. (2023b). NEMO source code to reproduce simulations presented in Bruciaferri et al. 2023—Submitted to Journal of Advances in Modeling Earth Systems (JAMES) [Software]. Zenodo. <https://zenodo.org/record/8056285>
- Bruciaferri, D. (2023c). Supporting data to reproduce figures and analysis presented in Bruciaferri et al. 2023—Submitted to Journal of Advances in Modeling Earth Systems (JAMES) [Dataset]. Zenodo. <https://zenodo.org/records/8055023>
- Bruciaferri, D., Shapiro, G., Stanichny, S., Zatsepin, A., Ezer, T., Wobus, F., et al. (2020). The development of a 3D computational mesh to improve the representation of dynamic processes: The Black Sea test case. *Ocean Modelling*, 146, 101534. <https://doi.org/10.1016/j.ocemod.2019.101534>
- Bruciaferri, D., Shapiro, G. I., & Wobus, F. (2018). A multi-envelope vertical coordinate system for numerical ocean modelling. *Ocean Dynamics*, 68(10), 1239–1258. <https://doi.org/10.1007/s10236-018-1189-x>
- Bruciaferri, D., Tonani, M., Ascione, I., Al Senafi, F., O’Dea, E., Hewitt, H. T., & Saulter, A. (2022). GULF18, a high-resolution NEMO-based tidal ocean model of the Arabian/Persian Gulf. *Geoscientific Model Development*, 15(23), 8705–8730. <https://doi.org/10.5194/gmd-15-8705-2022>
- Burchard, H., Petersen, O., & Petersen, O. (1997). Hybridization between σ - and z-co-ordinates for improving the internal pressure gradient calculation in marine models with steep bottom slopes. *International Journal for Numerical Methods in Fluids*, 25(9), 1003–1023. [https://doi.org/10.1002/\(SICI\)1097-0363\(19971115\)25:9\(1003::AID-FLD600\)3.0.CO;2-E](https://doi.org/10.1002/(SICI)1097-0363(19971115)25:9(1003::AID-FLD600)3.0.CO;2-E)
- Colombo, P. (2018). Modelling dense water flows through sills in large scale realistic ocean models: Demonstrating the potential of a hybrid geopotential/terrain-following vertical coordinate. Doctoral dissertation. Université Grenoble Alpes. Retrieved from <http://www.theses.fr/2018GREAU017>
- Colombo, P., Barnier, B., Penduff, T., Chanut, J., Deshayes, J., Molines, J.-M., et al. (2020). Representation of the Denmark Strait overflow in a z-coordinate eddy configuration of the NEMO (v3.6) ocean model: Resolution and parameter impacts. *Geoscientific Model Development*, 13(7), 3347–3371. <https://doi.org/10.5194/gmd-13-3347-2020>
- Cox, M. (1987). Isopycnal diffusion in a z-coordinate ocean model. *Ocean Modelling*, 74(1), 5.
- Cushman-Roisin, B., & Beckers, J.-M. (2011). In R. Dmowska, D. Hartmann, & H. T. Rossby (Eds.), *Introduction to geophysical fluid dynamics—Physical and numerical aspects* (2nd ed., p. 875).
- Daniault, N., Mercier, H., Lherminier, P., Sarafanov, A., Falina, A., Zunino, P., et al. (2016). The northern North Atlantic Ocean mean circulation in the early 21st century. *Progress in Oceanography*, 146, 142–158. <https://doi.org/10.1016/j.pocean.2016.06.007>
- Debreu, L., Kevlahan, N.-R., & Marchesiello, P. (2020). Brinkman volume penalization for bathymetry in three-dimensional ocean models. *Ocean Modelling*, 145, 101530. <https://doi.org/10.1016/j.ocemod.2019.101530>
- Debreu, L., Kevlahan, N.-R., & Marchesiello, P. (2022). Improved Gulf Stream separation through Brinkman penalization. *Ocean Modelling*, 179, 102121. <https://doi.org/10.1016/j.ocemod.2022.102121>
- Debreu, L., Marchesiello, P., Penven, P., & Cambon, G. (2012). Two-way nesting in split-explicit ocean models: Algorithms, implementation and validation. *Ocean Modelling*, 49–50, 1–21. <https://doi.org/10.1016/j.ocemod.2012.03.003>
- Debreu, L., Vouland, C., & Blayo, E. (2008). AGRIF: Adaptive grid refinement in Fortran. *Computers & Geosciences*, 34(1), 8–13. <https://doi.org/10.1016/j.cageo.2007.01.009>
- Dickson, R. R., & Brown, J. (1994). The production of North Atlantic deep water: Sources, rates, and pathways. *Journal of Geophysical Research*, 99(C6), 12319–12341. <https://doi.org/10.1029/94JC00530>
- R. R. Dickson, J. Meincke, & P. Rhines (Eds.). (2008). *Arctic–subarctic ocean fluxes*. Springer Netherlands. <https://doi.org/10.1007/978-1-4020-6774-7>
- Dukhovskoy, D. S., Morey, S. L., Martin, P. J., O’Brien, J. J., & Cooper, C. (2009). Application of a vanishing, quasi-sigma, vertical coordinate for simulation of high-speed, deep currents over the Sigsbee Escarpment in the Gulf of Mexico. *Ocean Modelling*, 28(4), 250–265. <https://doi.org/10.1016/j.ocemod.2009.02.009>
- Dukowicz, J. K., & Smith, R. D. (1994). Implicit free-surface method for the Bryan-Cox-Semtner ocean model. *Journal of Geophysical Research*, 99(C4), 7991–8014. <https://doi.org/10.1029/93JC03455>
- Ezer, T. (2005). Entrainment, diapycnal mixing and transport in three-dimensional bottom gravity current simulations using the Mellor–Yamada turbulence scheme. *Ocean Modelling*, 9(2), 151–168. <https://doi.org/10.1016/j.ocemod.2004.06.001>
- Ezer, T. (2006). Topographic influence on overflow dynamics: Idealized numerical simulations and the Faroe Bank Channel overflow. *Journal of Geophysical Research*, 111(C2), C02002. <https://doi.org/10.1029/2005JC003195>
- Ezer, T. (2016). Revisiting the problem of the Gulf Stream separation: On the representation of topography in ocean models with different types of vertical grids. *Ocean Modelling*, 104, 15–27. <https://doi.org/10.1016/j.ocemod.2016.05.008>
- Ezer, T., Arango, H., & Shchepetkin, A. F. (2002). Developments in terrain-following ocean models: Intercomparisons of numerical aspects. *Ocean Modelling*, 4(3–4), 249–267. [https://doi.org/10.1016/S1463-5003\(02\)00003-3](https://doi.org/10.1016/S1463-5003(02)00003-3)
- Ezer, T., & Mellor, G. L. (1994). Diagnostic and prognostic calculations of the North Atlantic circulation and sea level using a sigma coordinate ocean model. *Journal of Geophysical Research*, 99(C7), 14159–14171. <https://doi.org/10.1029/94JC00859>
- Ezer, T., & Mellor, G. L. (2004). A generalized coordinate ocean model and a comparison of the bottom boundary layer dynamics in terrain-following and in z-level grids. *Ocean Modelling*, 6(3–4), 379–403. [https://doi.org/10.1016/S1463-5003\(03\)00026-X](https://doi.org/10.1016/S1463-5003(03)00026-X)
- Gibson, A. (2019). *An adaptive vertical coordinate for idealised and global ocean modelling*. Doctoral dissertation. The Australian National University. <https://doi.org/10.25911/5f58b0768dafb>

- Good, S. A., Martin, M. J., & Rayner, N. A. (2013). EN4: Quality controlled ocean temperature and salinity profiles and monthly objective analyses with uncertainty estimates. *Journal of Geophysical Research: Oceans*, *118*(12), 6704–6716. <https://doi.org/10.1002/2013JC009067>
- Griffies, S. M. (2004). *Fundamentals of ocean climate models*. Princeton University Press.
- Griffies, S. M. (2012). *Elements of the modular ocean model (MOM): 2012 release (GFDL ocean group technical report No. 7) (Technical Report)*. NOAA/Geophysical Fluid Dynamics Laboratory.
- Griffies, S. M., Adcroft, A., & Hallberg, R. W. (2020). A primer on the vertical Lagrangian-remap method in ocean models based on finite volume generalized vertical coordinates. *Journal of Advances in Modeling Earth Systems*, *12*(10). <https://doi.org/10.1029/2019MS001954>
- Griffies, S. M., Böning, C., Bryan, F. O., Chassignet, E. P., Gerdes, R., Hasumi, H., et al. (2000). Developments in ocean climate modelling. *Journal of Computational Physics*, *2*(3–4), 123–192. [https://doi.org/10.1016/S1463-5003\(00\)00014-7](https://doi.org/10.1016/S1463-5003(00)00014-7)
- Griffies, S. M., Gnanadesikan, A., Pacanowski, R. C., Larichev, V. D., Dukowicz, J. K., & Smith, R. D. (1998). Isonutral diffusion in a z-coordinate ocean model. *Journal of Physical Oceanography*, *28*(5), 805–830. [https://doi.org/10.1175/1520-0485\(1998\)028<0805:IDIAZC>2.0.CO;2](https://doi.org/10.1175/1520-0485(1998)028<0805:IDIAZC>2.0.CO;2)
- Griffies, S. M., Pacanowski, R. C., & Hallberg, R. W. (2000). Spurious diapycnal mixing associated with advection in a z-coordinate ocean model. *Monthly Weather Review*, *128*(3), 538–564. [https://doi.org/10.1175/1520-0493\(2000\)128<0538:SDMAWA>2.0.CO;2](https://doi.org/10.1175/1520-0493(2000)128<0538:SDMAWA>2.0.CO;2)
- Guo, C., Ilicak, M., Bentsen, M., & Fer, I. (2016). Characteristics of the Nordic Seas overflows in a set of Norwegian Earth system model experiments. *Ocean Modelling*, *104*, 112–128. <https://doi.org/10.1016/j.ocemod.2016.06.004>
- Haidvogel, D., & Beckmann, A. (1999). *Numerical ocean circulation modeling*. Imperial College Press. <https://doi.org/10.2277/0521781825>
- Haney, R. L. (1991). On the pressure gradient force over steep topography in sigma coordinate ocean models. *Journal of Physical Oceanography*, *21*(4), 610–619. [https://doi.org/10.1175/1520-0485\(1991\)021<0610:otpgfo>2.0.co;2](https://doi.org/10.1175/1520-0485(1991)021<0610:otpgfo>2.0.co;2)
- Hansen, B., Larsen, K. M. H., Olsen, S. M., Quadfasel, D., Jochumsen, K., & Østerhus, S. (2018). Overflow of cold water across the Iceland–Faroe Ridge through the Western Valley. *Ocean Science*, *14*(4), 871–885. <https://doi.org/10.5194/os-14-871-2018>
- Hansen, B., & Østerhus, S. (2000). North Atlantic–Nordic Seas exchanges. *Progress in Oceanography*, *45*(2), 109–208. [https://doi.org/10.1016/S0079-6611\(99\)00052-X](https://doi.org/10.1016/S0079-6611(99)00052-X)
- Harada, Y., Kamahori, H., Kobayashi, C., Endo, H., Kobayashi, S., Ota, Y., et al. (2016). The JRA-55 reanalysis: Representation of atmospheric circulation and climate variability. *Journal of the Meteorological Society of Japan. Ser. II*, *94*(3), 269–302. <https://doi.org/10.2151/jmsj.2016-015>
- Harle, J. (2023). NEMO source code to reproduce the GOSI-szt vertical grid presented in Bruciaferri et al. 2023—Submitted to Journal of Advances in Modeling Earth Systems (JAMES) [Software]. Zenodo. <https://zenodo.org/record/8055445>
- Hirt, C., Amsden, A., & Cook, J. (1974). An arbitrary Lagrangian–Eulerian computing method for all flow speeds. *Journal of Computational Physics*, *14*(3), 227–253. [https://doi.org/10.1016/0021-9991\(74\)90051-5](https://doi.org/10.1016/0021-9991(74)90051-5)
- Hofmeister, R., Burchard, H., & Beckers, J. M. (2010). Non-uniform adaptive vertical grids for 3D numerical ocean models. *Ocean Modelling*, *33*(1–2), 70–86. <https://doi.org/10.1016/j.ocemod.2009.12.003>
- Holliday, N. P., Cunningham, S. A., Johnson, C., Gary, S. F., Griffiths, C., Read, J. F., & Sherwin, T. (2015). Multidecadal variability of potential temperature, salinity, and transport in the eastern subpolar North Atlantic. *Journal of Geophysical Research: Oceans*, *120*(9), 5945–5967. <https://doi.org/10.1002/2015JC010762>
- Hopkins, J. E., Holliday, N. P., Rayner, D., Houpert, L., Le Bras, I., Straneo, F., et al. (2019). Transport variability of the Irminger Sea deep western boundary current from a mooring array. *Journal of Geophysical Research: Oceans*, *124*(5), 3246–3278. <https://doi.org/10.1029/2018JC014730>
- Horn, R. A., & Johnson, C. R. (1985). *Matrix analysis*. Cambridge University Press. <https://doi.org/10.1017/CBO9780511810817>
- Hughes, S., Turrell, W., Hansen, B., & Østerhus, S. (2006). *Fluxes of Atlantic Water (volume, heat and salt) through the Faroe Shetland Channel calculated using a decade of acoustic Doppler current profiler data (1994–2005)*. Collaborative Report 01/06. Fisheries Research Services (Vol. 77). Marine Laboratory.
- Ilicak, M., Adcroft, A. J., Griffies, S. M., & Hallberg, R. W. (2012). Spurious diapycnal mixing and the role of momentum closure. *Ocean Modelling*, *45–46*, 37–58. <https://doi.org/10.1016/j.ocemod.2011.10.003>
- Jochumsen, K., Köllner, M., Quadfasel, D., Dye, S., Rudels, B., & Valdimarsson, H. (2015). On the origin and propagation of Denmark Strait overflow water anomalies in the Irminger Basin. *Journal of Geophysical Research: Oceans*, *120*(3), 1841–1855. <https://doi.org/10.1002/2014JC010397>
- Johns, W. E., Devana, M., Houk, A., & Zou, S. (2021). Moored observations of the Iceland–Scotland overflow plume along the eastern flank of the Reykjanes Ridge. *Journal of Geophysical Research: Oceans*, *126*(8), e2021JC017524. <https://doi.org/10.1029/2021JC017524>
- Johnson, H. L., Cessi, P., Marshall, D. P., Schloesser, F., & Spall, M. A. (2019). Recent contributions of theory to our understanding of the Atlantic meridional overturning circulation. *Journal of Geophysical Research: Oceans*, *124*(8), 5376–5399. <https://doi.org/10.1029/2019JC015330>
- Kasahara, A. (1974). Various vertical coordinate systems used for numerical weather prediction. *Monthly Weather Review*, *102*(7), 509–522. [https://doi.org/10.1175/1520-0493\(1974\)102<0509:VVCSUF>2.0.CO;2](https://doi.org/10.1175/1520-0493(1974)102<0509:VVCSUF>2.0.CO;2)
- Käse, R. H., Girton, J. B., & Sanford, T. B. (2003). Structure and variability of the Denmark Strait overflow: Model and observations. *Journal of Geophysical Research*, *108*(C6), 3181. <https://doi.org/10.1029/2002JC001548>
- Kieke, D., & Rhein, M. (2006). Variability of the overflow water transport in the western subpolar North Atlantic, 1950–97. *Journal of Physical Oceanography*, *36*(3), 435–456. <https://doi.org/10.1175/JPO2847.1>
- Kobayashi, S., Ota, Y., Harada, Y., Ebata, A., Moriya, M., Onoda, H., et al. (2015). The JRA-55 reanalysis: General specifications and basic characteristics. *Journal of the Meteorological Society of Japan. Ser. II*, *93*(1), 5–48. <https://doi.org/10.2151/jmsj.2015-001>
- Laanaia, N., Wirth, A., Molines, J. M., Barnier, B., & Verron, J. (2010). On the numerical resolution of the bottom layer in simulations of oceanic gravity currents. *Ocean Science*, *6*(2), 563–572. <https://doi.org/10.5194/os-6-563-2010>
- Large, W. G., & Yeager, S. G. (2009). The global climatology of an interannually varying air–sea flux data set. *Climate Dynamics*, *33*(2–3), 341–364. <https://doi.org/10.1007/s00382-008-0441-3>
- Leclair, M., & Madec, G. (2011). z-coordinate, an Arbitrary Lagrangian–Eulerian coordinate separating high and low frequency motions. *Ocean Modelling*, *37*(3–4), 139–152. <https://doi.org/10.1016/j.ocemod.2011.02.001>
- Legg, S., Briegleb, B., Chang, Y., Chassignet, E. P., Danabasoglu, G., Ezer, T., et al. (2009). Improving oceanic overflow representation in climate models: The gravity current entrainment climate process team. *Bulletin of the American Meteorological Society*, *90*(5), 657–670. <https://doi.org/10.1175/2008BAMS2667.1>
- Legg, S., Hallberg, R. W., & Girton, J. B. (2006). Comparison of entrainment in overflows simulated by z-coordinate, isopycnal and non-hydrostatic models. *Ocean Modelling*, *11*(1–2), 69–97. <https://doi.org/10.1016/j.ocemod.2004.11.006>
- Lemarié, F., Kurian, J., Shchepetkin, A. F., Jeroen Molemaker, M., Colas, F., & McWilliams, J. C. (2012). Are there inescapable issues prohibiting the use of terrain-following coordinates in climate models? *Ocean Modelling*, *42*, 57–79. <https://doi.org/10.1016/j.ocemod.2011.11.007>

- Levier, B., Treguier, A. M., Madec, G., & Garnier, V. (2007). *Free surface and variable volume in the NEMO code*. (Technical Report). Brest, France, MESRSEA IP report WP09-CNRS-STR03-1. IFREMER.
- Li, F., Lozier, M. S., Bacon, S., Bower, A., Cunningham, S., de Jong, M., et al. (2023). *Temperature, salinity and velocity data derived from the OSNAP array between August 2014 and May 2018*. (Technical Report). Georgia Institute of Technology. School of Earth and Atmospheric Sciences. <https://doi.org/10.35090/gatech/70328>
- Lozier, M. S., Bacon, S., Bower, A. S., Cunningham, S. A., Femke de Jong, M., de Steur, L., et al. (2017). Overturning in the subpolar North Atlantic program: A new international ocean observing system. *Bulletin of the American Meteorological Society*, 98(4), 737–752. <https://doi.org/10.1175/BAMS-D-16-0057.1>
- Lozier, M. S., Li, F., Bacon, S., Bahr, F., Bower, A. S., Cunningham, S. A., et al. (2019). A sea change in our view of overturning in the subpolar North Atlantic. *Science*, 363(6426), 516–521. <https://doi.org/10.1126/science.aau6592>
- Lozier, S. M., Bower, A. S., Furey, H. H., Drouin, K. L., Xu, X., & Zou, S. (2022). Overflow water pathways in the North Atlantic. *Progress in Oceanography*, 208, 102874. <https://doi.org/10.1016/j.pocean.2022.102874>
- Madec, G., & NEMO-team. (2019). *NEMO ocean engine* (Vol. 27). Scientific Notes of Climate Modelling Center, Institut Pierre-Simon Laplace (IPSL). <https://doi.org/10.5281/zenodo.3878122>
- Madec, G., Delecluse, P., Crépon, M., & Lott, F. (1996). Large-scale preconditioning of deep-water formation in the northwestern Mediterranean Sea. *Journal of Physical Oceanography*, 26(8), 1393–1408. [https://doi.org/10.1175/1520-0485\(1996\)026<1393:LSPODW>2.0.CO;2](https://doi.org/10.1175/1520-0485(1996)026<1393:LSPODW>2.0.CO;2)
- Martinho, A. S., & Batteen, M. L. (2006). On reducing the slope parameter in terrain-following numerical ocean models. *Ocean Modelling*, 13(2), 166–175. <https://doi.org/10.1016/j.ocemod.2006.01.003>
- Marzocchi, A., Hirschi, J. J.-M., Holliday, N. P., Cunningham, S. A., Blaker, A. T., & Coward, A. C. (2015). The North Atlantic subpolar circulation in an eddy-resolving global ocean model. *Journal of Marine Systems*, 142, 126–143. <https://doi.org/10.1016/j.jmarsys.2014.10.007>
- Mastropole, D., Pickart, R. S., Valdimarsson, H., Våge, K., Jochumsen, K., & Girtton, J. (2017). On the hydrography of Denmark Strait. *Journal of Geophysical Research: Oceans*, 122(1), 306–321. <https://doi.org/10.1002/2016JC012007>
- McCarthy, G. D., Brown, P. J., Flagg, C. N., Goni, G., Houpert, L., Hughes, C. W., et al. (2020). Sustainable observations of the AMOC: Methodology and technology. *Reviews of Geophysics*, 58(1), e2019RG000654. <https://doi.org/10.1029/2019RG000654>
- Megann, A., Chanut, J., & Storkey, D. (2022). Assessment of the z time-filtered arbitrary Lagrangian-Eulerian coordinate in a global eddy-permitting ocean model. *Journal of Advances in Modeling Earth Systems*, 14(11). <https://doi.org/10.1029/2022MS003056>
- Megann, A., New, A. L., Blaker, A. T., & Sinha, B. (2010). The sensitivity of a coupled climate model to its ocean component. *Journal of Climate*, 23(19), 5126–5150. <https://doi.org/10.1175/2010JCLI3394.1>
- Mellor, G. L., Ezer, T., & Oey, L.-Y. (1994). The pressure gradient conundrum of sigma coordinate ocean models. *Journal of Atmospheric and Oceanic Technology*, 11(4), 1126–1134. [https://doi.org/10.1175/1520-0426\(1994\)011<1126:TPGCOS>2.0.CO;2](https://doi.org/10.1175/1520-0426(1994)011<1126:TPGCOS>2.0.CO;2)
- Mellor, G. L., Oey, L. Y., & Ezer, T. (1998). Sigma coordinate pressure gradient errors and the seamount Problem. *Journal of Atmospheric and Oceanic Technology*, 15(5), 1122–1131. [https://doi.org/10.1175/1520-0426\(1998\)015<1122:SCPGEA>2.0.CO;2](https://doi.org/10.1175/1520-0426(1998)015<1122:SCPGEA>2.0.CO;2)
- O’Dea, E. J., Arnold, A. K., Edwards, K. P., Furner, R., Hyder, P., Martin, M. J., et al. (2012). An operational ocean forecast system incorporating NEMO and SST data assimilation for the tidally driven European North-West shelf. *Journal of Operational Oceanography*, 5(1), 3–17. <https://doi.org/10.1080/1755876X.2012.1102012>
- Østerhus, S., Woodgate, R., Valdimarsson, H., Turrell, B., de Steur, L., Quadfasel, D., et al. (2019). Arctic Mediterranean exchanges: A consistent volume budget and trends in transports from two decades of observations. *Ocean Science*, 15(2), 379–399. <https://doi.org/10.5194/os-15-379-2019>
- Pacanowski, R. C., Gnanadesikan, A., & Olume, V. (1998). Transient response in a Z-level ocean model that resolves topography with partial cells. *Monthly Weather Review*, 126(12), 3248–3270. [https://doi.org/10.1175/1520-0493\(1998\)126<3248:TRIAZL>2.0.CO;2](https://doi.org/10.1175/1520-0493(1998)126<3248:TRIAZL>2.0.CO;2)
- Penduff, T., Le Sommer, J., Barnier, B., Treguier, A.-M., Molines, J.-M., & Madec, G. (2007). Influence of numerical schemes on current-topography interactions in 1/4° global ocean simulations. *Ocean Science*, 3(4), 509–524. <https://doi.org/10.5194/os-3-509-2007>
- Petersen, M. R., Jacobsen, D. W., Ringler, T. D., Hecht, M. W., & Maltrud, M. E. (2015). Evaluation of the arbitrary Lagrangian–Eulerian vertical coordinate method in the MPAS-ocean model. *Ocean Modelling*, 86, 93–113. <https://doi.org/10.1016/j.ocemod.2014.12.004>
- Phillips, N. A. (1957). A coordinate system having some special advantages for numerical forecasting. *Journal of Meteorology*, 14(2), 184–185. [https://doi.org/10.1175/1520-0469\(1957\)014<0184:ACSHSS>2.0.CO;2](https://doi.org/10.1175/1520-0469(1957)014<0184:ACSHSS>2.0.CO;2)
- Quadfasel, D. (2018). *Physical oceanography during POSEIDON cruise POS503*. PANGAEA. <https://doi.org/10.1594/PANGAEA.890699>
- Rattan, S., Myers, P. G., Treguier, A.-M., Theetten, S., Biastoch, A., & Böning, C. (2010). Towards an understanding of Labrador Sea salinity drift in eddy-permitting simulations. *Ocean Modelling*, 35(1–2), 77–88. <https://doi.org/10.1016/j.ocemod.2010.06.007>
- Riemenschneider, U., & Legg, S. (2007). Regional simulations of the Faroe Bank Channel overflow in a level model. *Ocean Modelling*, 17(2), 93–122. <https://doi.org/10.1016/j.ocemod.2007.01.003>
- Saunders, P. M. (1996). The flux of dense cold overflow water southeast of Iceland. *Journal of Physical Oceanography*, 26(1), 85–95. [https://doi.org/10.1175/1520-0485\(1996\)026<0085:TFODCO>2.0.CO;2](https://doi.org/10.1175/1520-0485(1996)026<0085:TFODCO>2.0.CO;2)
- Schoonover, J., Dewar, W., Wienders, N., Gula, J., McWilliams, J. C., Molemaker, M. J., et al. (2016). North Atlantic barotropic vorticity balances in numerical models. *Journal of Physical Oceanography*, 46(1), 289–303. <https://doi.org/10.1175/JPO-D-15-0133.1>
- Seim, K. S., Ferberntsen, I. J., & Berntsen, J. (2010). Regional simulations of the Faroe Bank Channel overflow using a σ -coordinate ocean model. *Ocean Modelling*, 35(1–2), 31–44. <https://doi.org/10.1016/j.ocemod.2010.06.002>
- Shapiro, G. I., Luneva, M., Pickering, J., & Storkey, D. (2013). The effect of various vertical discretization schemes and horizontal diffusion parameterization on the performance of a 3-D ocean model: The Black Sea case study. *Ocean Science*, 9(2), 377–390. <https://doi.org/10.5194/os-9-377-2013>
- Shchepetkin, A. F., & McWilliams, J. C. (2005). The regional oceanic modeling system (ROMS): A split-explicit, free-surface, topography-following-coordinate oceanic model. *Ocean Modelling*, 9(4), 347–404. <https://doi.org/10.1016/j.ocemod.2004.08.002>
- Song, Y., & Haidvogel, D. (1994). A semi-implicit ocean circulation model using a generalized topography-following coordinate system. *Journal of Computational Physics*, 115(1), 228–244. <https://doi.org/10.1006/jcph.1994.1189>
- Stacey, M. W., Pond, S., & Nowak, Z. P. (1995). A numerical model of the circulation in Knight Inlet, British Columbia, Canada. *Journal of Physical Oceanography*, 25(6), 1037–1062. [https://doi.org/10.1175/1520-0485\(1995\)025<1037:ANMOTC>2.0.CO;2](https://doi.org/10.1175/1520-0485(1995)025<1037:ANMOTC>2.0.CO;2)
- Storkey, D., Blaker, A. T., Mathiot, P., Megann, A., Aksenov, Y., Blockley, E. W., et al. (2018). UK global ocean GO6 and GO7: A traceable hierarchy of model resolutions. *Geoscientific Model Development*, 11(8), 3187–3213. <https://doi.org/10.5194/gmd-11-3187-2018>
- Timmermann, R., Wang, Q., & Hellmer, H. (2012). Ice-shelf basal melting in a global finite-element sea-ice/ice-shelf/ocean model. *Annals of Glaciology*, 53(60), 303–314. <https://doi.org/10.3189/2012AoG60A156>
- Treguier, A. M., Theetten, S., Chassignet, E. P., Penduff, T., Smith, R., Talley, L., et al. (2005). The North Atlantic subpolar gyre in four high-resolution models. *Journal of Physical Oceanography*, 35(5), 757–774. <https://doi.org/10.1175/JPO2720.1>

- Wang, H., Legg, S. A., & Hallberg, R. W. (2015). Representations of the Nordic Seas overflows and their large scale climate impact in coupled models. *Ocean Modelling*, 86, 76–92. <https://doi.org/10.1016/j.ocemod.2014.12.005>
- Wang, Q., Danilov, S., Sidorenko, D., Timmermann, R., Wekerle, C., Wang, X., et al. (2014). The finite element sea ice-ocean model (FESOM) v.1.4: Formulation of an ocean general circulation model. *Geoscientific Model Development*, 7(2), 663–693. <https://doi.org/10.5194/gmd-7-663-2014>
- Willebrand, J., Barnier, B., Böning, C., Dieterich, C., Killworth, P. D., Le Provost, C., et al. (2001). Circulation characteristics in three eddy-permitting models of the North Atlantic. *Progress in Oceanography*, 48(2–3), 123–161. [https://doi.org/10.1016/S0079-6611\(01\)00003-9](https://doi.org/10.1016/S0079-6611(01)00003-9)
- Winton, M., Hallberg, R., & Gnanadesikan, A. (1998). Simulation of density-driven frictional downslope flow in Z-coordinate ocean models. *Journal of Physical Oceanography*, 28(11), 2163–2174. [https://doi.org/10.1175/1520-0485\(1998\)028<2163:SODDFD>2.0.CO;2](https://doi.org/10.1175/1520-0485(1998)028<2163:SODDFD>2.0.CO;2)
- Wise, A., Harle, J., Bruciaferri, D., O’Dea, E., & Polton, J. (2021). The effect of vertical coordinates on the accuracy of a shelf sea model. *Ocean Modelling*, 170, 101935. <https://doi.org/10.1016/j.ocemod.2021.101935>
- Xu, X., Bower, A., Furey, H., & Chassignet, E. P. (2018). Variability of the Iceland-Scotland overflow water transport through the Charlie-Gibbs fracture zone: Results from an eddy simulation and observations. *Journal of Geophysical Research: Oceans*, 123(8), 5808–5823. <https://doi.org/10.1029/2018JC013895>
- Xu, X., Schmitz, W. J., Hurlburt, H. E., Hogan, P. J., & Chassignet, E. P. (2010). Transport of Nordic Seas overflow water into and within the Irminger Sea: An eddy-resolving simulation and observations. *Journal of Geophysical Research*, 115(C12), C12048. <https://doi.org/10.1029/2010JC006351>